FLUID INJECTED COOLING SYSTEMS FOR HYPERSONIC RE-ENTRY VEHICLES

Undergraduate Thesis

Presented in Partial Fulfillment of the Requirements for Graduation with Research Distinction in the Department of Aerospace and Aeronautical Engineering

At The Ohio State University

By:

Nathaniel J. Alspach

April 2016

Advisor: Dr. Datta Gaitonde

ABSTRACT

Re-entry into the earth's atmosphere, or any atmospheric body, is an arduous task. High heat loads, intense deceleration, and chemically reactive flows make this a difficult environment to model and design for. Typically a great deal of foresight is needed as to what the physics of the flow and the trajectory the vehicle will take beforehand. The current state-of-the-art technologies are adequate at handling the thermal and chemical environments found in such flows, but require precise timing and positioning to ensure the vehicle follows a predetermined trajectory with a narrow margin for error. This rapidly becomes problematic for missions when such conditions are not known beforehand or some change is made to the mission profile. For this reason it is novel to have a cooling system that is capable of adapting to changing flight conditions and mission requirements. The purpose of this study is to determine the effectiveness of a Fluid Injection Cooling System (FICS) as a substitute for a standard heat shield on reentry vehicles. The reentry vehicle considered is the Orion Crew Module, part of the Orion Multi-Purpose Crew Vehicle being developed by NASA. The FICS for this study is a single cold-gas injector situated at the stagnation point of the capsule, with Helium and Nitrogen being tested as the injected gasses. The FICS reduces reentry heating through three mechanisms: increasing bow-shock standoff distance, absorbing heat and creating an inert buffer around the capsule. Increasing the standoff distance favorably alters the shock geometry to reduce heat transfer to the capsule. The cool-gas/fluid also absorbs heat from the much hotter external flow. Finally, the inert buffer created by the FICS helps protect the capsule from free radical oxygen molecules which can erode the capsule and interfere with the communication system.

This paper investigates the effectiveness of such a system by using computational modeling of the flow in ANSYS FLUENT v.16 with post processing being done in CFD POST v.16 using an axisymmetric model of the re-entry vehicle to reduce computation time and data needs. Data collected in this study is processed by use of non-dimensional parameters so that the results of this study can be used on scaled models for validation and can be applied to a wide range of flow regimes. The procedure of forming non-dimensional parameters will also allow the results of this study to be implemented in control algorithms that could correct for deviations from the planned trajectory.

ACKNOWLEDGEMENTS

There are many people whom I would like to give my full acknowledgement to here, but if I did, then this section would likely be longer than my thesis itself. Therefore, I will limit myself to recognizing those most directly involved with my research.

First and foremost, I would like to thank my Advisor, Dr. Datta Gaitonde, for the immense amount of support and insight that he has provided to me over the duration of this process, and for the encouragement he has given me to continue pursuing my studies at the graduate level. Computational Fluid Dynamics can be incredibly frustrating and is filled with enormous pitfalls in time, where weeks may be spent trying to resolve an issue that takes a few mouse clicks to mitigate. His guidance has saved me from days, or even weeks, of grief during the course of my thesis, and has helped to keep my spirits up during this ordeal.

I would also like to thank Dr. Mazumder and Dr. Chen, both of whom have taught me Computational Fluid Dynamics techniques and theory that will be used liberally in this text. Dr. Chen's lessons have helped me to understand the theory behind the techniques and their limitations in implementation. After writing my own CFD codes for him during my time in his course, I was able to better understand the challenges I would face in obtaining a converged solution, and had a grasp of the software I was using beyond the basics of the interface. Dr. Mazumder's course has taught me the specifics of how Fluent works as software, as well as the finer points of meshing and post processing. His willingness to give me lecture material in advance, so that I may incorporate into my own models in Fluent, has saved me a tremendous amount of work and has helped me to obtain the results that will be presented in this paper.

My teammates in my senior capstone project also deserve special recognition here. Zac Pressler, Allen Roe, Colin Nautly, Wes Straw, and Ryan Little have all provided me with friendship and comradery throughout this ordeal, and have helped me to keep my head up and marching forward throughout the past year. Without their help I would likely not have been able to complete this paper at all. They have shared in my workload, and have had the temperament to handle my various eccentricities. I owe them all a debt of gratitude, and probably pizza too.

I would also like to thank my parents and grandfather. Both of my parents have encouraged my pursuit of engineering my whole life, and have always supported me, even when things became difficult. They taught me to put one hundred percent of my effort into everything I do, and it has paid off in dividends. My grandfather was my original inspiration to become an engineer. Hours spent tinkering in his workshop instilled a passion in me to discover how the world works, and I would not be the person I am today without him.

Lastly, I would like to thank my girlfriend, Emily Schueller. She was the one who encouraged me to do thesis research in the first place, and has pushed me to work harder. Her love and support have encouraged me to expand outside my normal comfort zone, and has allowed me to reach goals I didn't think myself capable of.

TABLE OF CONTENTS

LIST OF FIGURES

LIST OF TABLES

CHAPTER 1: INTRODUCTION

Chapter 1.1: Focus of Research

During atmospheric reentry, the tremendous heat generated around a reentry vehicle often exceeds the melting point of most conventional materials. Traditional methods for dealing with reentry heating involve using ablative shielding composed of specialized materials, to carry away heat when descending through the atmosphere. After descent, what is left of the heat shielding material must be removed and replaced, which can be expensive and time consuming. For example, the Space Shuttle was a reusable vehicle that was meant to have a lifespan of nearly 100 launches but required replacement of the heat shield material after each launch. This intensive procedure led servicing technicians to disassemble, check, and usually replace other components of the Space Shuttle which contributed to the increase in cost per launch from the proposed $20 million to nearly $1.6 billion per launch over the life of the Space Shuttle program [NASA's Shuttle Program Cost $209 Billion - Was It Worth It?].

Another means for protecting against reentry heating is using thermal soak heat shields, which absorb heat into the material itself, dissipating it by convection or radiation over the duration of the descent. Even thermal soak heat shields, which are designed to avoid the costly and time-intensive procedures typical of ablative heat shields, still require regular repairs or replacements due to micrometeoroid impacts, warping due to thermal stresses in the material, and normal degradation known as “popcorning”, where weaknesses in the material propagate along material discontinuities along the metal or ceramic grains. Furthermore, once within the

atmosphere, the descent profile of a reentry capsule cannot be meaningfully altered in flight by traditional heat shields. The Space Shuttle incorporated wings to provide such maneuverability but in turn suffered additional weight penalties. In general, lifting body type designs like that of the Space Shuttle fly higher in the atmosphere for a longer duration, which lowers the peak heat flux on the vehicle and peak deceleration, but at the expense of the total heat load on the shield. [Atmospheric Re-Entry]. Despite these inefficiencies, these approaches for cooling reentry vehicles have remained fundamentally unchanged since the 1960s. In order to have truly reusable reentry vehicles, new methods that are cheaper, require less maintenance time and offer additional capabilities must be developed.

A fluid injection cooling system (FICS) that provides heat shielding via film cooling could be a viable alternative to conventional heat shielding. The FICS uses cool gas/fluid that is injected through outlets or vents across the surface of the vehicle to reduce the heat transferred from the hot, high-speed flow and protect the reentry capsule. Fluid injection could also offer a method for maneuvering the reentry vehicle during descent and, thus, greater control over the descent profile and landing locations, similar to control methods used for conventional ballistic capsules [An Automated Method to Compute Orbital Re-entry Trajectories with Heating Constraints]. A computational model validated by empirical models described in similar papers [Aerothermal Analysis of a Sample-Return Reentry Capsule] [Calculation of Reentry-Vehicle Temperature History] will be constructed in order to test the

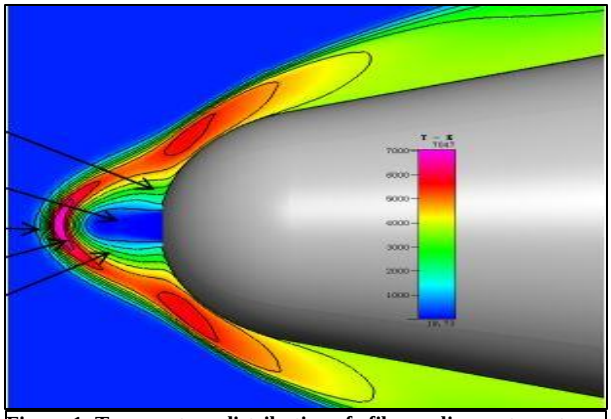

Figure 1: Temperature distribution of afilm cooling system at Mach 20 [Film Cooling Effectiveness For Hypersonic Vehicles]

effectiveness of the proposed FICS, in comparison to conventional heat shields. Specifically, the Sutton-Graves, Tauber, Gilbert and Scala, and Detra Hidalgo models will be used to this effect. These models can then be used to make a direct comparison between the proposed FICS and other traditional heat shields [Development of Thermal Protection Systems of The MUSES-C/DASH Reentry Capsule] [Aerothermal Analysis of a Sample-Return Reentry Capsule] as well as similar systems described in prior research [Film Cooling Effectiveness For Hypersonic Vehicles] [Effect of Counterflow Jet on a Supersonic Reentry Capsule].

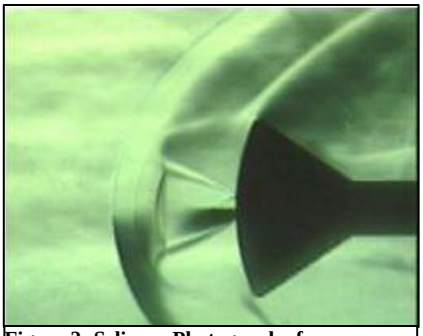

Figure 2: Sclieren Photograph of a Counterflow Jet over an Apollo Capsule [Effect of Counterflow Jet on a Supersonic Reentry Capsule]

Chapter 1.2: Significance of Research

The ability to adjust the trajectory and heating of a re-entry vehicle during descent cannot be understated. With such narrow margins for success, the ability to correct the course of a capsule in ballistic descent can mean the difference between a safe landing and a complete mission failure. This distinction is particularly pronounced in manned and military applications, where failure may not be an option. Though some methods exist in conventional re-entry vehicles to correct their trajectory mid-flight [An Automated Method to Compute Orbital Re-entry Trajectories with Heating Constraints] [Atmospheric Re-Entry], they are limited in that they cannot control the heat dissipation rate as well as the trajectory, leaving the two coupled, and making design of such systems a much more arduous task. By using a cold gas injected into the front of the shock wave, the level of heat dissipation can be adjusted as needed, while conventional methods can be used to provide additional control and steering. In addition to the benefits a controllable method of heat dissipation, the injection of liquid helium and other gasses

will help to lower the concentrations of monatomic oxygen near the capsule walls, which can block out communications and erode the structure of the reentry vehicle. This type of heat shield also has the added benefit of being able to be refueled after use and reused for additional atmospheric descents, a feature that comes in handy in for single stage to orbit (SSTO) applications. The research presented also offers an improvement over existing works, since the vehicle being investigated is the Orion Capsule, which is a more current design than those presented in other works [Film Cooling Effectiveness For Hypersonic Vehicles] [Effect of Counterflow Jet on a Supersonic Reentry Capsule]. In addition to this, the aforementioned studies do not report their results in non-dimensional parameters, whereas this one does. The use of non-dimensional parameters will allow the results of this study to be applied to other similar geometries, or allow the descent vehicle in question to be operated in atmospheres other than earths, which is novel considering that the intended use of this particular vehicle is for both the terrestrial and Martian atmospheres. Analysis conducted in this manner is also well suited to use in a closed loop control system for similar reasons, and makes this technique useful for missions where conditions may not be known beforehand, or where drastic trajectory changes are necessary to avoid obstacles or collision. Such capabilities lend themselves well to a wide variety of scientific, civilian, and military applications. The results of this study can also be extended to hypersonic atmospheric vehicles which may employ the use of active cooling in their designs, such as the recently proposed SABRE space plane, or SR-72, both of which would travel within the flight envelope that will be studied in this paper.

Chapter 1.3: Overview of Thesis

The remainder of this paper will explore the methodology implemented and the results obtained from this study, namely the mathematical models, meshing, and assumptions used to simulate the flow and the effect of the injected fluid has on things like the drag, heat flux, and temperature of the capsule wall based on the mass flow rate of the injected fluid, altitude, and free stream velocity. In reality, other parameters such as the thermal, momentum, and mass diffusivity affect the flow and can change the drag, heat flux, and temperature distribution, but their affect is not as influential to these dependent parameters as the mass flow rate of the injected fluid, altitude, and free stream velocity. The dependent and independent parameters of significance have been formed into non-dimensional number in the following manner:

Independent parameters:

1) $Free\ Stream\ Mach\ Number \equiv M_\infty = \frac{u_\infty}{\sqrt{\gamma R T_\infty}}$

2) $Free\ Stream\ Reynolds\ Number \equiv Re_\infty = \frac{\rho_\infty u_\infty D_{capsule}}{\mu_\infty}$

3) $Injected\ Reynolds\ Number \equiv Re_{inlet} = \frac{\pi \dot{m}_{inlet}}{4\mu_\infty D_{inlet}}$

Dependent parameters:

4) $Drag\ Coefficient \equiv C_D = \frac{2F_{drag}}{\rho u_\infty^2}$

5) $Nusselt\ Number \equiv Nu_D = \frac{hD_{capsule}}{k_\infty}$

6) $Eckert\ Number \equiv Ec = \frac{u_\infty^2}{c_{p\infty}(T_0 - T_\infty)}$

The mathematical models that will be used to simulate the flow are a highly coupled system of partial differential equations that describe the flow conditions via the conservation of mass, momentum, and energy in an axisymmetric model using a density based Roe solver that utilizes a conservative form of the fundamental equations. The simulation uses NIST real gas laws and Fickian diffusion to model the numerous species present in the flow, as well as the injected gas, and treats the front of the capsule as an isothermal wall with a thermal conductivity approximately that of tungsten. The turbulence model that is used is a K-epsilon model, which is much less computationally intensive than RANS and Large Eddie models or Direct Numerical Simulations, but at the cost of some accuracy. Because of the difficulty of modeling a chemically reactive flow over a complex geometry, the initial results of this study were conducted over a spherical geometry, where the meshing requirements were simpler to satisfy and validation was easier to conduct, due to the abundance of literature available on spheres in high speed flows. Additional results were compiled for the Orion Capsule geometry and will be presented below. However, the chemical modeling of the flow will not be incorporated into the results presented, and cold flows will represent the bulk of the data. The results presented represent a data set that tests the characteristics of the heat shield over Reynolds numbers ranging from 10,000 to 1,000,000 and Mach numbers ranging from 5 to 10. Though this does not capture the full scope of reentry profiles that the capsule may experience, and the chemical reactions represent a significant amount of heat dissipation within the flow, the modeling of such extreme conditions is computationally intensive, beyond what the computers available to this researcher can handle in reasonable time frames. Most re-entry vehicles begin their descent at

speeds in excess of Mach 25, but do so through highly rarified air, where the assumption of continuity employed in the mathematical model is not necessarily valid. However, since the chemical reactions within the flow are primarily endothermic, the results of the cold gas flow simulations will give a more conservative estimate of the total amount of energy dissipated by the flows interaction with the capsule. Therefore, this paper seeks to establish the methods that would be employed if such computational power were available, and will present results to validate that the model would be sufficient to model such conditions, as well as preliminary results for the chemically active flow that will serve the basis for future research.

CHAPTER 2: MATHEMATICAL MODELING

Chapter 2.1: Roe Density based Solver

To understand how the Roe Density based solver is employed in this paper, it is critical to have an understanding of how the fundamental Navier Stokes equations governing it are formed. In most cases, this is either in a conservative form, where all relevant quantities interest are tracked from a fixed control volume, and the non-conservative form, where the control volume moves with the fluid itself and the mass contained within the control volume is conserved. These different forms of the fundamental equations can be further broken down into their integral and derivative forms. For the solver used in this study, a finite volume approach is employed, which is to say that the state variables at any given point in the flow are calculating by approximating the integral over the control volume in consideration in a fixed control volume. Therefore the integral form of the Navier Stokes equations is of interest to us in this case:

7) $Conservation\ of\ Mass \equiv \frac{\partial}{\partial t}\iiint_{\Sigma} \rho\, \partial\forall + \oiint_{\partial\Sigma} \rho\vec{V}\cdot\overrightarrow{\partial S} = 0$

8) $Conservation\ of\ Momentum \equiv \frac{\partial}{\partial t}\iiint_{\Sigma} \rho\vec{V}\, \partial\forall + \oiint_{\partial\Sigma} \rho\vec{V}(\vec{V}\cdot\vec{n}) + P\vec{n}\, \partial S = \iiint_{\Sigma} \rho\vec{f}$

9) $Conservation\ of\ Energy$

$$\equiv \frac{\partial}{\partial t}\iiint_{\Sigma} \rho\left(e + \frac{|\vec{V}|^2}{2}\right)\partial\forall + \oiint_{\partial\Sigma}\left(\rho\left(e + \frac{|\vec{V}|^2}{2}\right)(\vec{V}\cdot\vec{n}) + P\vec{V}\cdot\vec{n}\right)\partial S = 0$$

10) $Equation\ of\ State \equiv P = \rho\frac{R_u T}{\mathcal{M}}$

The Navier Stokes equations in this form are not conducive for numerical solutions in a compressible flow however. This is because compressible flows, especially the hypersonic flows considered in this paper, are discontinuous across shocks. These sharp changes in temperature, velocity, and density cannot be accurately modeled when the domain is discretized into cells via first and second order numerical approximations. Using the equations in their current form would result in numerical errors accumulating due to the dramatic, nearly instantaneous change over the shock, which would in turn cause the solution to diverge even for an implicit solver. For this reason, the equations are formed into their conservative form, which consists of flux terms that are conserved across the boundary of the shock. The equations in their conservative Cartesian form are presented below:

11) $$Conservative\ Navier\ Stokes \equiv \frac{\partial U}{\partial t} + \frac{\partial F(U)}{\partial x} + \frac{\partial G(U)}{\partial y} + \frac{\partial H(U)}{\partial z} = J$$

12) $$U = \left(\rho \quad \rho u \quad \rho v \quad \rho w \quad \rho\left(e + \frac{\left|\vec{V}\right|^2}{2}\right)\right)^T$$

13) $$F = \left(\rho u \quad \rho u^2 + P - \tau_{xx} \quad \rho v u - \tau_{xy} \quad \rho w u - \tau_{xz} \quad \rho\left(e + \frac{\left|\vec{V}\right|^2}{2}\right)u + \rho u - k\frac{\partial T}{\partial x} - u\tau_{xx} - v\tau_{xy} - w\tau_{xz}\right)^T$$

14) $$G = \left(\rho v \quad \rho u v - \tau_{yx} \quad \rho v^2 + P - \tau_{yy} \quad \rho w v - \tau_{yz} \quad \rho\left(e + \frac{\left|\vec{V}\right|^2}{2}\right)v + \rho v - k\frac{\partial T}{\partial y} - u\tau_{yx} - v\tau_{yy} - w\tau_{yz}\right)^T$$

15) $H = \left(\rho w \quad \rho uw - \tau_{zx} \quad \rho vw - \tau_{zy} \quad \rho w^2 + P - \tau_{zz} \quad \rho\left(e + \frac{|\vec{V}|^2}{2}\right)w + \rho w - k\frac{\partial T}{\partial z} - u\tau_{zx} - v\tau_{zy} - w\tau_{zz}\right)^T$

16) $J = \begin{pmatrix} 0 & \rho f_x & \rho f_y & \rho f_x & \rho\left(uf_x + vf_y + wf_z + \dot{q}\right) \end{pmatrix}^T$

However, the model presented in this paper uses an axisymmetric assumption to lower the computational requirements of the simulation by reducing the total number of equations that need to be solved for. Therefore, the conservative Navier Stokes equations in their cylindrical coordinate form will be presented below for the sake of completeness, but the remaining discussion on the Roe solver following them will be presented using the Cartesian forms of the equations:

17) $Conservative\ Cylindrical\ Navier\ Stokes \equiv \frac{\partial U}{\partial t} + \frac{\partial A}{\partial z} + \frac{\partial B}{\partial r} + \frac{\partial C}{r\partial\theta} + \frac{D}{r} = 0$

18) $A =$
$(\rho u_z \quad \rho u_z^2 + P - \tau_{zz} \quad \rho u_z u_r - \tau_{rz} \quad \rho u_z u_\theta - \tau_{\theta z} \quad \rho h u_z - u_z\tau_{zz} - u_r\tau_{rz} - u_\theta\tau_{\theta z} + \dot{q}_z)^T$

19) $B =$
$(\rho u_r \quad \rho u_r u_z - \tau_{zr} \quad \rho u_r^2 + P - \tau_{rr} \quad \rho u_r u_\theta - \tau_{\theta r} \quad \rho h u_r - u_z\tau_{zr} - u_r\tau_{rr} - u_\theta\tau_{\theta r} + \dot{q}_r)^T$

20) $C =$
$(\rho u_\theta \quad \rho u_\theta u_z - \tau_{z\theta} \quad \rho u_\theta u_r - \tau_{r\theta} \quad \rho u_\theta^2 + P - \tau_{\theta z} \quad \rho h u_\theta - u_z\tau_{z\theta} - u_r\tau_{r\theta} - u_\theta\tau_{\theta\theta} + \dot{q}_\theta)^T$

21) $D =$
$\left(\rho u_r \quad \rho u_z u_r - \tau_{rz} \quad \rho\left(u_r^2 - u_\theta^2\right) - \tau_{rr} + \tau_{\theta\theta} \quad 2\rho u_r u_\theta - 2\tau_{\theta r} \quad \rho h u_r - u_z\tau_{zr} - u_r\tau_{rr} - u_\theta\tau_{\theta r} + \dot{q}_r\right)^T$

22) $U = (\rho \quad \rho u_z \quad \rho u_r \quad \rho u_\theta \quad \rho h)^T$

The Roe solvers method of discretization of these equations is a two-step process. First the chain rule is applied to the conservative form of the fundamental equations to obtain a Jacobian matrix that represents them in a state space and then this Jacobian is made constant over a discrete interval, thus linearizing them. For the sake of discussion the process by which this is conducted will be shown for the x direction of the flow only, since the other coordinate directions are handled in similar manners. The process by which the fundamental equations are formed into Jacobian matrices and subsequently linearized proceeds as follows [Dr. C. P. Dullemond Max-Planck-Institut fuer Astronomie]:

$$23)\ U_t + F(U)_x = 0 \iff U_t + \Lambda(U)U_x = 0 \iff U_t + \tilde{\Lambda}U_x, \qquad \Lambda(Q) = \frac{\partial F}{\partial U}$$

$$24)\ \Lambda = \begin{bmatrix} 0 & 1 & 0 & 0 & 0 \\ \hat{\gamma}h - u^2 - a^2 & (3-\gamma)u & -\hat{\gamma}v & -\hat{\gamma}w & \hat{\gamma} \\ -uv & v & u & 0 & 0 \\ -uw & w & 0 & u & 0 \\ \frac{1}{2}u[(\gamma-3)h - a^2] & h - \hat{\gamma}u^2 & -\hat{\gamma}uv & -\hat{\gamma}uw & \gamma u \end{bmatrix}$$

$$25)\ \hat{\gamma} = \gamma - 1\ , \qquad a = \sqrt{\gamma P/\rho}$$

Where the eigenvalues and eigenvectors of the Jacobian are as follows:

$$26)\ \lambda_1 = u - a, \qquad \lambda_2 = \lambda_3 = \lambda_4 = u, \qquad \lambda_5 = u + a$$

$$27)\ \vec{\xi}_1 = \begin{bmatrix} 1 \\ u-a \\ v \\ w \\ h - ua \end{bmatrix}, \qquad \vec{\xi}_2 = \begin{bmatrix} 1 \\ u \\ v \\ w \\ \frac{V^2}{2} \end{bmatrix}, \qquad \vec{\xi}_3 = \begin{bmatrix} 0 \\ 0 \\ 1 \\ 0 \\ v \end{bmatrix}, \qquad \vec{\xi}_4 = \begin{bmatrix} 0 \\ 0 \\ 0 \\ 1 \\ w \end{bmatrix}, \qquad \vec{\xi}_5 = \begin{bmatrix} 1 \\ u+a \\ v \\ w \\ h + ua \end{bmatrix}$$

These constant value Jacobian matrices are formed together by the solver into a global matrix and global state vector, which is then solved using typical methods employed in matrix solvers, such as the Gauss Seidel method, or in very particular cases where the problem is defined in such

a way that a tridiagonal matrix is formed, the Thomas Algorithm. In order for the constant value matrices to accurately represent the original Jacobian matrix, they must satisfy several criteria which affect how they are formed. The discretized matrix and the original Jacobian must share eigenvalues at every index, the Jacobian and discretized matrix must have the same index values at any given node in the mesh, and the difference in flux vectors at any two adjacent nodes must be equal to the value of the discretized matrix when it is made to be a function of the difference in the conservative state vector at those two adjacent nodes. The numerical representation of these criteria and how they are met proceeds as follows [Dr. C. P. Dullemond Max-Planck-Institut fuer Astronomie]:

28) $\widetilde{\lambda_i} = \widetilde{\lambda_i}(U_l, U_r) \in \mathbb{R}, \forall i$

29) $\widetilde{\Lambda}(U, U) = \Lambda(U)$

30) $F(U_r) - F(U_l) = \widetilde{\Lambda}(U_r - U_l)$

31) $\tilde{u} = \dfrac{\sqrt{\rho_l}u_l + \sqrt{\rho_r}u_r}{\sqrt{\rho_l} + \sqrt{\rho_r}}$

32) $\tilde{v} = \dfrac{\sqrt{\rho_l}v_l + \sqrt{\rho_r}v_r}{\sqrt{\rho_l} + \sqrt{\rho_r}}$

33) $\tilde{w} = \dfrac{\sqrt{\rho_l}w_l + \sqrt{\rho_r}w_r}{\sqrt{\rho_l} + \sqrt{\rho_r}}$

34) $\tilde{h} = \dfrac{\sqrt{\rho_l}h_l + \sqrt{\rho_r}h_r}{\sqrt{\rho_l} + \sqrt{\rho_r}}$

35) $\tilde{V}^2 = \tilde{u}^2 + \tilde{v}^2 + \tilde{w}^2$

36) $\tilde{a} = \hat{\gamma}\sqrt{\tilde{h} - \dfrac{\tilde{V}^2}{2}}$

One important consideration that should be noted here is that the previous systems of equations shown were all transient, while the results of this study are conducted assuming a steady state solution to the flow. This is because the transient portion of the equations are used to update the solution in most computational fluid dynamic solver schemes because of the nature of the Navier Stokes equations themselves. If one were to treat these equations in their steady state form and attempt to iterate over geometric space, problems would rapidly arise because of the stark difference in the nature of the mathematical model before and after the shock. Subsonic and transonic flows tend to have an elliptic behavior when they are steady, meaning that the solution to one point in the computational domain is coupled with all others. Conversely, the fluid in the supersonic portion of the flow is governed by parabolic equations which are coupled only to fluid that is upstream of the point in consideration. This provides great difficulties in obtaining a solution, because the location of the shock affects how results will be obtained in different parts of the flow, but the method for obtaining those results is required to find the location of the shock in most cases. With the exception of well poised problems, where the analytical or numerical solution is either simplified or known from experimental data, this makes it nearly impossible to solve such problems. However, when transient terms are introduced, the equations become hyperbolic in every part of the domain, which is even more favorable than if they were parabolic, as the size of the computational domain is decreased between iterations compared to parabolic equations. Most solvers use a sort of time step between iterations to march the solution towards convergence, which is determined by the Courant-Friedrichs-Lewy number (CFL number) and the relaxation factors applied to the solver.

The Roe Solver is widely used in simulation of compressible flows in computational fluid dynamics because of its simplicity and robustness across a wide variety of flow regimes. It is

particularly useful since it is a shock capturing scheme, meaning that the location of the shock need not be known beforehand, and that reduces the amount of time that must be devoted to meshing [Dr. C. P. Dullemond Max-Planck-Institut fuer Astronomie]. Though it does not enjoy some of the advantages of a higher order scheme like the MUSCL-Hancock method, or the ability to handle multiphase flows without knowing the eigenvalue structure, like the AUSM method, it is one of the most researched and extensively used algorithms for this type of flow problem. For this reason, it is the solver of choice for this paper.

Chapter 2.2: K-Epsilon and K-Omega Turbulence Models

During Reentry through the earth's atmosphere, the vast majority of deceleration of a re-entry vehicle occurs under free stream conditions that are normally considered to be laminar for vehicles traveling at low Mach numbers, since the flow about the vehicle tends to be highly rarified, with Reynolds numbers on the order of 10,000, which is well below the commonly used transition Reynolds number of 2,000,000 for external flows. However, beneath the shock the flow deaccelerates rapidly and density, pressure, and temperature increase significantly. At the surface of the capsule, the local Reynolds number can reach as high as 3,800,000 [Laminar-Turbulent Transition on Reentry Capsules and Planetary Probes], well past the critical Reynolds number necessary to induce turbulence. In addition to this, even when the local Reynolds number is well below the critical Reynolds number at all points along the capsule, turbulent flow can still be induced by odd geometric features such as radiator fins, RCS

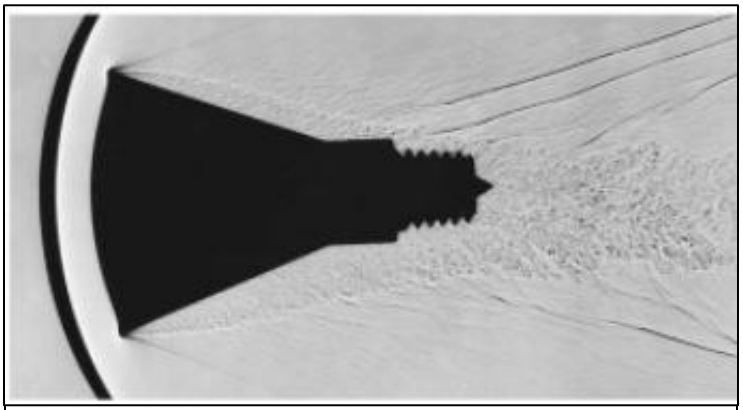

Figure 3: Turbulent flow over Mercury capsule at Mach 3.28 [Free-Flight Measurements of Static and Dynamic Stability of Models of the Project Mercury Re-Entry Capsule at Mach Numbers 3 and 9.5]

ports, windows, hatches, or structural features like those on the Mercury and Gemini capsules. Therefore it is necessary to model such effects on the capsule despite free stream conditions suggesting otherwise.

Modeling turbulent flow is a subject that can cover the span of entire books, and often entire papers are written concerning just that single aspect of the flow in question. Turbulence governs flow phenomena at every single scale of flow in a given problem, ranging from large eddies that can occupy significant portions of the dynamic energy in a given fluid, to eddies on the Kolmogorov scale, where the validity of the continuity assumption employed in most computational fluid dynamics models begins to be called into question, as the Kolmogorov scale can sometimes be on the order of the length of the mean free path of the molecules in the flow. This kind of computationally intensive modeling is far beyond the scope of what this author wishes to present in this paper, and would involve resources and time that is simply not available to anything but devoted studies of the subject of turbulence itself. Therefore, this study will focus itself on two models in particular that are popular in commercial applications of turbulence modeling, namely the k-ϵ and k-ω models. Both models employ the use of two additional equations to model the flow, which provide a much more simplistic model of the turbulence at the cost of not being able to resolve the physics of the flow at smaller length scales.

The k-ϵ model uses the turbulent kinetic energy (k) of the flow and the dissipation (ϵ) to model the turbulence in the flow, which is one of the simplest models for which only initial or boundary conditions are needed. It is often poorly suited for curved boundary layers, or ones where the pressure gradient is large, but variants of the model that correct for curvature exist. Also, because the turbulent portion of the flow is behind the bow shock, the pressure gradients in the most important portions of the flow for this papers consideration are modest. The equations

governing the most generally employed variant of the k-ϵ model are as follows in Einstein notation:

$$37)\ \frac{\partial(\rho k)}{\partial t} + \frac{\partial(\rho k u_i)}{\partial x_i} = \frac{\partial}{\partial x_j}\left[\frac{\mu_t}{\sigma_k}\frac{\partial k}{\partial x_j}\right] + 2\mu_t E_{ij}^2 - \rho\epsilon$$

$$38)\ \frac{\partial(\rho\epsilon)}{\partial t} + \frac{\partial(\rho\epsilon u_i)}{\partial x_i} = \frac{\partial}{\partial x_j}\left[\frac{\mu_t}{\sigma_\epsilon}\frac{\partial\epsilon}{\partial x_j}\right] + C_{1\epsilon}\frac{\epsilon}{k}2\mu_t E_{ij}^2 - C_{2\epsilon}\rho\frac{\epsilon^2}{k}$$

$$39)\ \mu_t = \rho C_\mu \frac{k^2}{\epsilon}$$

$$40)\ C_\mu = 0.09, \qquad \sigma_k = 1, \qquad \sigma_\epsilon = 1.3, \qquad C_{1\epsilon} = 1.44, \qquad C_{2\epsilon} = 1.92$$

The k-ω model of turbulence is quite similar to k-ϵ model in both its formulation and its wide use in computational fluid dynamics with a few noted differences. While the k-ϵ model uses the dissipation rate of turbulent kinetic energy, the k-ω model uses the specific dissipation rate of turbulent kinetic energy instead. It also has a better handling of adverse pressure gradients and is more suitable for transitionary flows from laminar to turbulent, whereas the k-ϵ model is generally better suited to flows that are fully turbulent. However, this research has shown that the k-ω model tends to have a slower convergence when compared to the k-ϵ model, and gives less conservative estimates of pressure losses due to viscous effects. The equations governing the most generally employed variant of the k-ω model are as follows in Einstein notation:

$$41)\ \frac{\partial(\rho k)}{\partial t} + \frac{\partial(\rho k u_i)}{\partial x_i} = \frac{\partial}{\partial x_j}\left(\Gamma_k\frac{\partial k}{\partial x_j}\right) + G_k - Y_k + S_k$$

$$42)\ \frac{\partial(\rho\omega)}{\partial t} + \frac{\partial(\rho\omega u_i)}{\partial x_i} = \frac{\partial}{\partial x_j}\left(\Gamma_\omega\frac{\partial\omega}{\partial x_j}\right) + G_\omega - Y_\omega + S_\omega$$

43) $Effective\ Diffusivities$: $\Gamma_k = \mu + \frac{\mu_t}{\sigma_k}, \qquad \Gamma_\omega = \mu + \frac{\mu_t}{\sigma_\omega}$

44) $Turbulent\ Viscosity \equiv \mu_t = \alpha^* \frac{\rho k}{\omega}$

45) $Diffusivity\ correction$: $\alpha^* = \alpha_\infty^* \left(\frac{\alpha_0^* + Re_t/R_k}{1 + Re_t/R_k} \right), \qquad Re_t = \frac{\rho k}{\mu \omega}$

46) $Production\ rates$: $G_k = 2\mu_t E_{ij}^2, \qquad G_\omega = \alpha \frac{\omega}{k} G_k$

47) $Production\ Correction$: $\alpha = \frac{\alpha_\infty}{\alpha^*} \left(\frac{\alpha_0 + Re_t/R_\omega}{1 + Re_t/R_\omega} \right)$

48) $Dissipation$: $Y_k = \rho \beta^* f_{\beta^*} k\omega, \qquad Y_w = \rho \beta f_\beta \omega^2$

49) $f_{\beta^*} = \begin{cases} 1 & \chi_k \leq 0 \\ \frac{1 + 680\chi_k^2}{1 + 400\chi_k^2} & \chi_k > 0 \end{cases}, \qquad f_\beta = \frac{1 + 70\chi_\omega}{1 + 80\chi_\omega}$

50) $\chi_k = \frac{1}{\omega^3} \frac{\partial k}{\partial x_j} \frac{\partial \omega}{\partial x_j}, \qquad \chi_\omega = \left| \frac{\Omega_{ij} \Omega_{jk} E_{ki}}{(\beta_\infty^* \omega)^3} \right|$

51) $\beta^* = \beta_i^* [1 + \zeta^* F(M_t)],\ \beta_i^* = \beta_\infty^* \left(\frac{4/15 + (Re_t/R_\beta)^4}{1 + (Re_t/R_\beta)^4} \right),\ \beta = \beta_i \left[1 - \frac{\beta_i^*}{\beta_i} \zeta^* F(M_t) \right]$

52) $E_{ij} = \frac{1}{2} \left(\frac{\partial u_j}{\partial x_i} + \frac{\partial u_i}{\partial x_j} \right), \qquad \Omega_{ij} = \frac{1}{2} \left(\frac{\partial u_i}{\partial x_j} - \frac{\partial u_j}{\partial x_i} \right)$

53) $Compressibility\ Correction$: $F(M_t) = \begin{cases} 0 & M_t \leq M_{t0} \\ M_t^2 - M_{t0}^2 & M_t > M_{t0} \end{cases}, \qquad M_t^2 = \frac{2k}{\alpha^2}$

54) $\alpha_\infty^* = 1,\ \alpha_\infty = 0.52,\ \alpha_0 = \frac{1}{9},\ \beta_\infty^* = 0.09,\ \beta_i = 0.072,\ R_\beta = 8,\ R_k = 6,\ R_\omega = 2.95,$

$\zeta^* = 1.5,\ M_{t0} = 0.25,\ \sigma_k = 2,\ \sigma_\omega = 2$

Both the turbulence models presented have advantages and disadvantages, and will both be used for comparison in the study, but the main model that will be employed will be the k-ϵ model, because it is simpler to implement since it doesn't rely on the calculation of the shear strain in the fluid as well as the normal strain, which would require the computing of the fluid curl as well as the divergence instead of just the fluid divergence. Realistically, the choice of turbulence models in this paper is a best choice of which answer is less wrong, since neither fully captures the full physics of the turbulent flow, and neither is completely accurate in their treatment of the transition from laminar to turbulent flow. For this reason other considerations, like the computation requirements of the problem are more heavily weighted in the model choice until empirical data can be found for this particular reentry vehicle to validate the model. In both models the constants used are gathered from past empirical data.

Regardless of the turbulence model chosen, the cell size near the wall of the capsule must be appropriately sized to ensure that the boundary layer of the flow is properly modeled. Turbulent boundary layers are treated as piecewise functions, where the initial layer is linear and the secondary layer is logarithmic. The optimal cell sizing is one that is able to capture the linear portion of the boundary layer within a single cell, so that the boundary layer about the geometry of interest is fully resolved. The approximation of the turbulent boundary layer is as follows:

$$55)\ \frac{u}{u_\tau} = \begin{cases} y_+ & y_+ \le 11 \\ 5 + 2.5 \ln y_+ & y_+ > 11 \end{cases}, \qquad y_+ = \frac{\rho u_\tau y}{\mu}, \qquad u_\tau = \sqrt{\frac{\tau_w}{\rho}}$$

This formulation of the boundary layers requires a wall shear stress, which must be obtained using information at the nodes closest to the wall of the geometry in consideration, but the spacing of the nodes is what these equations is trying to determine. Because the spacing of

the nodes near the wall will affect the result obtained for shear stress, and an iterative method to obtain the precise distance from the wall the nodes must be placed in order to optimize the solution would be computationally intensive and unlikely to converge, another method must be employed that can yield an answer that is reasonable for the purposes of initial mesh sizing. For this reason, an approximation of the wall shear stress is obtained using empirical relations based on the Reynolds number of the flow:

$$56)\ \tau_w = \frac{1}{2}\rho C_f u_\infty^2, \qquad C_f = 0.058 Re^{-\frac{1}{5}}$$

Chapter 2.3: Fick's Law and the Diffusion Model

The diffusion and concentration of various chemical species in a flow is of great importance to the study of hypersonic flows, as well as chemically reacting flows in general. Depending on the concentration of various chemical species, such as monatomic oxygen, nitrous oxides, or water vapor, the properties of the flow near features of interest in any model will change. This is especially true for properties like the viscosity, heat capacity, and thermal conductivity, which are all functions of the molecular properties of the gas in question, and thus are sensitive to the mixture contents of such gases. In hypersonic flows specifically, the concentration of monatomic oxygen, as seen in figure 4, is often of great concern since this particular species, as its name might suggest, tends to oxidize the surface of objects within the hypersonic free stream, which can reduce material strength. This same species is also the culprit

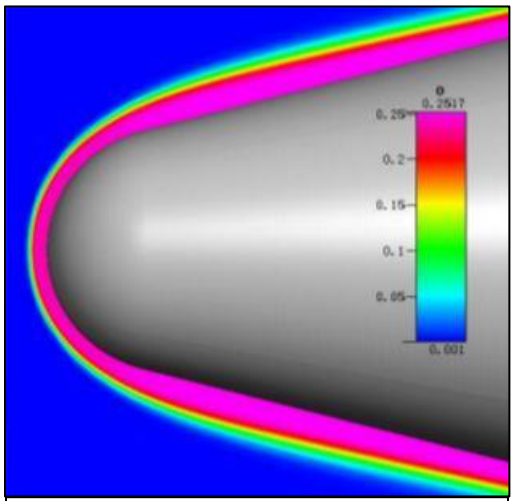

Figure 4: Oxygen mass concentration near blunt body walls. [Film Cooling Effectiveness for Hypersonic Vehicles]

behind communications losses during reentry, since monatomic oxygen in hypersonic flows is ionized, leaving free electrons to accrue on vital communication systems, introducing electrical interference [Film Cooling Effectiveness for Hypersonic Vehicles]. There exists a variety of different approaches to treating diffusion in computational models, but the most fundamental distinction between various models is whether they treat diffusion as an active or passive scalar. Models that treat the diffusion with passive scalars are less complex than those with active scalars, since the concentration of different species doesn't affect the flow strongly in such models, so calculations for diffusivity can be treated like a post processing step. While models like these may be adequate for flows where there are trace amounts of a certain species within a flow, it doesn't work well where there are high concentrations of species within the flow. For the problem considered in this paper, the inlet of the injector introduces species that aren't present in the free stream at high concentrations, so a passive model would be inadequate. This means all species within the flow considered should be treated as active scalars, which adds coupling between the flow and the concentration of species within the flow, so that the diffusion equations must be solved simultaneously with the fundamental flow equations and turbulence model. Diffusion models can be further separated into categories based on the number of species they handle, as well as whether they use mass fractions, volume fractions, or mole fractions. For their treatment in this paper, a mass fraction based model is used, which helps to aid the calculation of mass continuity as a measure of computational accuracy in the solver.

The conservation of species within the governing equations primarily affects the conservation of mass, but depending on whether or not reactions are included in the model, can influence the formulation of the entire set of governing equations of the flow. The governing equations with multiple species are as follows:

57) $Conservation\ of\ Mass$: $\frac{\partial}{\partial t}(\rho Y_i) + \nabla \cdot (\rho \vec{V} Y_i) = -\nabla \cdot \vec{J}_i + \dot{S}_i$

58) $Conservation\ of\ X\ Momentum$: $\frac{\partial}{\partial t}(\rho u) + \nabla \cdot (\rho u \vec{V}) = -\nabla \cdot \tau_x + \dot{S}_u$

59) $Conservation\ of\ Energy$: $\frac{\partial}{\partial t}(\rho c_p T) + \nabla \cdot (\rho c_p T \vec{V}) = \nabla \cdot (k \nabla T) + \dot{S}_h$

When reactions aren't considered, the $\dot{S}$ terms drop out, and only the mass conservation equation is affected. The treatment of the diffusion flux generally depends on how many species are being considered. For diffusion problems with two species being considered, Fick's law is adequate to handle the modeling of the flow:

60) $Fick's\ Law$: $J_i = \rho D_i \nabla Y_i$

61) $D_{ij} \approx \frac{1}{3} \bar{c} \lambda_{mfp} \sim \frac{T^{3/2}}{P}$

For non-binary diffusion problems, like the one presented in this paper, a more sophisticated treatment of the flow is needed. This is because the application of Fick's law results in conservation of mass being neglected, since diffusion coefficients for different species are not necessarily the same, leaving an un-canceled term in the right hand side of the mass conservation equation. To overcome the loss of mass continuity in the model, several methods can be employed. For systems where additional species are dilute, the dilute approximation can be used, which essentially treats the remaining species as passive scalars. For air, this approximation tends to work well, since the main constituents of the gas mixture are diatomic nitrogen and oxygen. However, for the gas mixture considered in this paper, the dilute approximation loses accuracy near the capsule walls, where large amounts of saturated vapor of

helium, water vapor, or other gases are being injected at high mass concentrations. To deal with multi species diffusion, the Stefan Maxwell diffusion equations must be employed:

$$62)\ \frac{\nabla \mu_i}{RT} = \nabla \ln a_i = \sum_{\substack{j=1 \\ j \neq i}}^{n} \frac{\chi_i \chi_j}{D_{ij}} (\vec{V}_j - \vec{V}_i) = \sum_{\substack{j=1 \\ j \neq i}}^{n} \frac{c_i c_j}{c^2 D_{ij}} \left(\frac{\vec{J}_j}{c_j} - \frac{\vec{J}_i}{c_i} \right)$$

Where μ_i is the chemical potential, a_i is the chemical activation, and c_i is the molar concentration. In addition to the treatment of multiple diffusion coefficients in the flow, the presence of thermal, or Soret diffusion should be treated to adequately model the heat transfer and mass transfer in the flow. Additionally, the treatment of turbulent diffusion is also of importance to this research paper. This modifies the normal Fick's diffusion law as follows:

$$63)\ J_i = -\left(\rho D_{i,m} + \frac{\mu_t}{Sc_t} \right) \nabla Y_i - \rho D_{T,i} \frac{\nabla T}{T}$$

$$64)\ Schmidt\ number \equiv Sc_t = \frac{\mu_t}{\rho D_t}$$

$$65)\ D_{i,m} = \frac{1 - \chi_i}{\sum_{j, j \neq i} (\chi_j / D_{ij})}$$

Where μ_t is the turbulent viscosity as it is defined in Equation 44, and D_t and $D_{T,i}$ are the turbulent and thermal diffusivity contributions respectively. The diffusivity coefficients are found through kinetic theory via a modified form of the Chapman-Enskog formula [Fluent Database]:

$$66)\ D_{ij} = 0.00188 \frac{\left[T^3 \left(\frac{1}{\mathcal{M}_i} + \frac{1}{\mathcal{M}_j} \right) \right]^{1/2}}{P \sigma_{ij}^2 \Omega_D}$$

67) $\Omega_D = f(T_D^*), \qquad T_D^* = \dfrac{T}{(\epsilon/k_B)_{ij}}, \qquad (\epsilon/k_B)_{ij} = \sqrt{(\epsilon/k_B)_i(\epsilon/k_B)_j}$

68) $\sigma_{ij} = \dfrac{1}{2}(\sigma_i + \sigma_j)$

The formulations for Lennard Jones parameters for the Chapman-Enskog equation are given in Equations 67 and 68, and are contained within Fluent's chemistry and mixture models. The presence of multiple species within the flow also influences the way in which fluid parameters are formed. There is also the effect of high temperatures in the flow that must be considered as well, since fluid parameters for the individual species are strongly functions of temperature, and the Soret diffusion further complicates things. The formulation of local fluid parameters, such as viscosity and heat capacity, are as follows [Mazumder's Lecture Notes] [Viscosity of Gas Mixtures]:

69) $\mu_{mix} = \sum_{i=1}^{n} \dfrac{\chi_i \mu_i}{\chi_i + \sum_{\substack{j=1 \\ j \neq i}}^{n} \varphi_{ij} \chi_j}$

70) $\varphi_{ij} = \alpha_{ij}\left[1 + \dfrac{\mathcal{M}_i - \mathcal{M}_j\left(\dfrac{\alpha_{ji}}{\alpha_{ij}}\right)^{1/2}}{\dfrac{3A_{ij}^*(\mathcal{M}_i + \mathcal{M}_j)}{5 - 3A_{ij}^*} + \dfrac{(\alpha_{ij})^{1/2} + (\alpha_{ji})^{1/2}}{1 + (\alpha_{ij}\alpha_{ji})^{1/2}}\mathcal{M}_j(\alpha_{ji})^{1/2}}\right]$

71) $\alpha_{ij} = \left(\dfrac{2\mathcal{M}_j}{\mathcal{M}_i + \mathcal{M}_j}\right)^{1/2}\left(\dfrac{\sigma_{ij}^2}{\sigma_i \sigma_j}\right)\dfrac{\sigma_j}{\sigma_i}$

72) $c_{p,i} = \begin{cases} K_{11} + K_{12}T + K_{13}T^2 + K_{14}T^3 + K_{15}T^4, & T_{min} \leq T < T_{break} \\ K_{21} + K_{22}T + K_{23}T^2 + K_{24}T^3 + K_{25}T^4, & T_{break} \leq T \leq T_{max} \end{cases}$

Chapter 2.4: Chemistry Considerations

Though this paper will not focus on the effects of chemical reactions in the hypersonic flow model, it is nevertheless important to discuss how such modeling would be conducted for future research considerations. The modeling of chemically reacting flows in low subsonic flows is fairly well understood. This is because the thermal aspects of the flow are dominated by the energy of the reactions, temperatures are still fairly low in comparison to hypersonic flows, and there isn't any complex flow phenomenon like shock waves to be dealt with. However, in this case, the thermal energy dissipated by the flow due to reactions is complicated by the presence of extremely high temperatures, which can cause dissociation as well as ionization of gas species, shock waves and large pressure gradients, whose shape is coupled with the chemical reactions themselves, and thick boundary layers that are commonly referred to as entropy layers in most texts on the subject. Because of these effects, the number of different chemical reactions that are occurring increases dramatically, and thus the number of species that must be tracked and the number of equations needed to model said species increases as well. In addition to the previously mentioned effects, the high energies within the molecules must be given additional treatment to conserve the accuracy of the chemical reactions and ionizations occurring. The prior section of this chapter showed a piecewise polynomial expression for the specific heat of a gas species. This treatment of specific heat attempts to resolve the way in which temperature and heat are related via an empirical approach. In reality, the reason for this temperature dependence of specific heat is because of the different mechanism by which energy is stored thermally within the molecule itself, namely in translational, rotational, and vibrational degrees of freedom. Because of this, the exchange of energy between these different energy carrying modes must be accounted for via Landau-Teller Theory [Chemical Modelling in Nonequilibrium

Hypersonic Flow Around Blunt Bodies]. The rotational and translational degrees of freedom do not have a significant effect on chemical reactions, but the vibrational modes, which emerge at higher temperatures, do have a non-negligible effect. These vibrational interactions are dependent on both temperature and pressure of the constituent species, making the highly coupled with the flow, making it impractical to treat the flow with piecewise functions as were previously described. In the model discussed in this paper, there are only three species being considered at any given time: N_2, O_2, and the injection fluid. However, if reactions were to be considered, there would be considerably more to be taken into account. A very simplified model of such reactions might have us considering additional species like N, O, NO, NO^+, and free radical electrons, as well as any species that may form from combination with the injection fluid. If just the free stream species are considered, and more complex reactions that may occur are ignored, then there is a total of 17 elementary reactions that must be tracked [Chemical Modelling in Nonequilibrium Hypersonic Flow Around Blunt Bodies]. This vastly complicates the system of equations that were previously being considered, and would make computation times much longer. For this reason, no further consideration will be given to such effects over the course of this paper.

CHAPTER 3: COMPUTATIONAL METHODOLOGY

Chapter 3.1: Meshing considerations

Meshing is often a difficult process in any computational fluid dynamic's problem. From low speed incompressible flows to the hypersonic flows considered in this paper, there are often a variety of competing considerations that must be taken into account. One of the most fundamental considerations is whether the mesh is to be structured or unstructured. Structured grids are those where the connectivity of the nodes and elements in the computational array is known implicitly. Structured grids use quadrilateral elements, or in three dimensional problems hexahedral elements, to represent the geometry of the object. Often structured meshes are divided into blocked regions that allow each blocked domain to be solved using a much smaller array that is coupled to adjacent blocks instead of solving the entire geometry in a large, sparsely filled array. Structured meshes typically take less time to converge and use up less memory as well. This is because for quadrilateral meshes have one unique node per element along the interior of a mesh, whereas tetrahedral meshes have two unique nodes per element along their interior. Structured meshes also have the advantage of being able to resolve things like boundary layers more easily, since their sizing and alignment normal to surfaces is easier to control. Structured meshes are usually fitted to curved surfaces using either Algebraic, or elliptic partial differential equation transforms, which can require a decent amount of processing power to set up. In contrast, most of the advantages associated with unstructured meshes come not from the computational savings or resolution they provide, but from the ease which they can be applied to complex geometries, and the quality of mesh that can be obtained by using triangular and tetrahedral elements. Because triangles are a simple shape that can be formed by any three

points that do not lie on the same line, meshing is far easier to accomplish than in structured meshes. More complex geometries can be broken down into a series of triangles, so this also makes it far easier to mesh geometries with enclosed curves. Unstructured meshes also benefit from the fact that transforms are not used to fit the mesh to the geometry in question, which decreases the amount of time needed to form the mesh and improves aspects of the quality like the skewedness and aspect ratio of the elements. This is because the algorithms used are designed to optimize quality directly instead of treating it as a post processing step after the fitting of the mesh to the curvature of the geometry is complete.

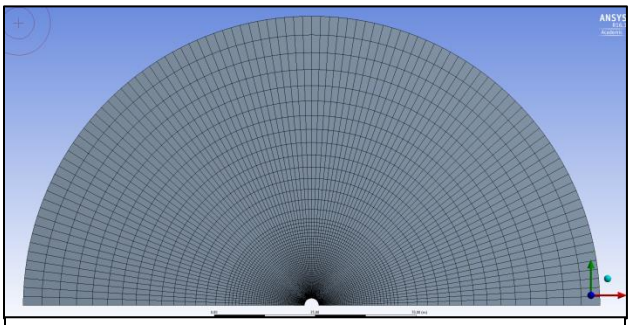

Figure 5: Structured mesh for a spherical body with two blocked regions

The main consideration when making the choice between a structured or unstructured grid is typically the geometry in question. In this case, the geometry of the capsule has sharp, discontinuous edges as well as smooth curves, so the meshing immediately around the capsule can be compromised by this. For geometries that are simple, or are smooth, structural meshes are ideal, and can produce great results. This is evident in Figure 4, where all elements are conformal because the geometry is fairly simple. However, structured meshes tend not to do well when the geometry involves multiple types of curves because they require different kinds of

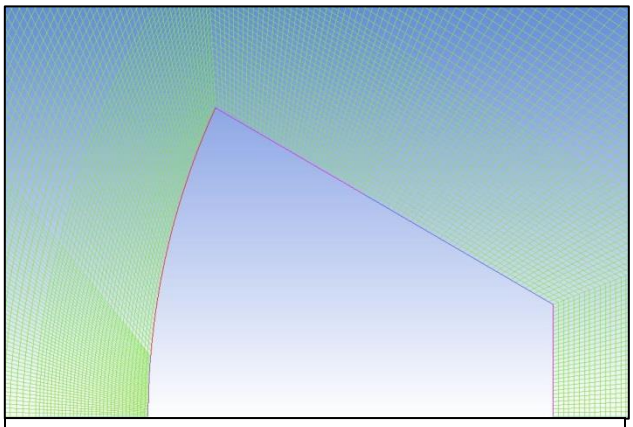

Figure 6: Structured mesh for the Orion capsule near the wall of the geometry.

transforms to treat them and sudden discontinuities tend to produce skewed elements, which have low mesh quality. This can be seen clearly in Figure 6, where the elements closest to the blocking have a high skewedness, and are not suitable for use in computation. They would most likely result in divergence of the solver, since the Jacobian of such elements is near zero. This can be resolved by creating a sufficiently large number of blockings to be able to resolve such features, or by creating guiding curves to associate the blocks to that do not represent the physical geometry itself. However, the types of curves needed to guide the mesh in a way that avoids skewedness of the elements requires either the use of method of characteristics to determine the shape of the curve or the use of more processing power to compute such curves via numerical methods. By using more blocks this can be done with one's intuition, but the number of blocks needed will require more processing and there is less margin for error in the setup of such a mesh.

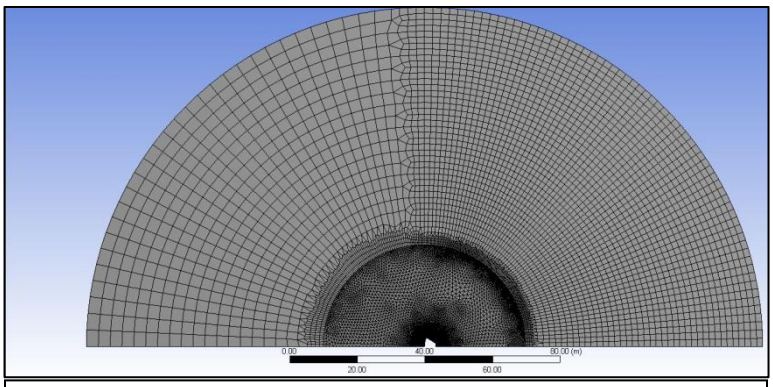

Figure 7: Hybrid mesh for the capsule geometry

The mesh used in this study is a composite of both varieties of mesh, which can be seen in Figure 7 above. It was designed to provide high mesh quality about the region closest to the capsule wall and converge quickly. This is because the mesh is divided into three distinct regions that are meshed independently of one another: the capsule near-field mesh, the fore far-field mesh, and the aft far-field mesh. Both the fore and aft far-field meshes are mainly structured quadrilateral meshes, with elements near the boundaries of the two being and the capsule near-field mesh being a mixture of both quadrilateral elements and triangular elements.

Elements along the boundaries, while quadrilateral dominant, are still unstructured and add computation time. The density of the fore far-field mesh is much lower than that of the aft far-field mesh, because the flow ahead of the bow shock is uniform and the wake that follows behind the capsule will reside in the aft far-field mesh. By keeping the mesh density in the fore far-field mesh lower and increasing it in the aft far-field mesh, the mesh places more elements of high quality where important features of the flow are known to be, and thus yields a higher accuracy result than a uniform mesh would for the same number of elements. The far-field meshes extend over 20 capsule diameters in all directions radially to make sure the boundary conditions used in the simulation are accurate. This is crucial to maintaining the accuracy of the simulation since the boundary conditions can radically alter the solution of the system of partial differential equations, even though the equations themselves have not changed. The near-field capsule mesh, as shown in Figure 8, is an unstructured triangular mesh. Because the turbulent boundary layer must be resolved in the way described in Chapter 2 Section 2, the sizing of the mesh is important to the accuracy of the solution. Unstructured meshes are particularly difficult to deal with in this regard, because the distance of

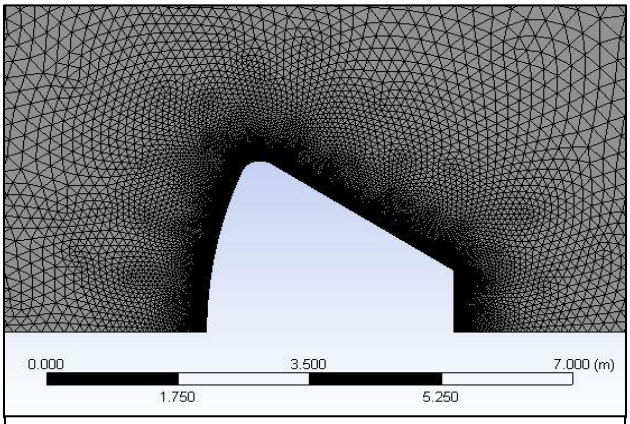

Figure 8: Unstructured mesh for the Orion capsule near the wall of the geometry.

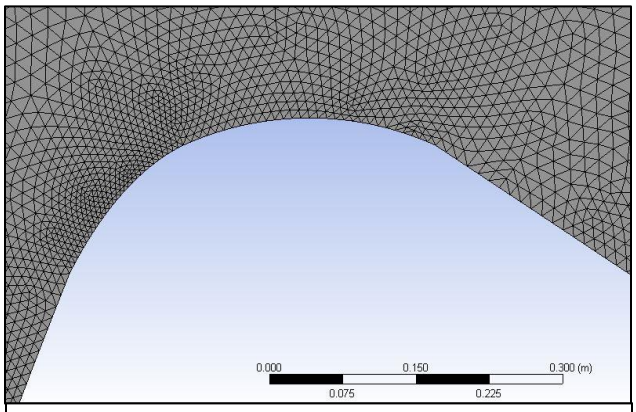

Figure 9: Unstructured mesh at the boundary of the capsule. Minimum mesh size is 0.5 cm.

each cell from the wall isn't uniform. This means that the minimum mesh density must be of a sufficient to resolve the boundary layer. Furthermore, the different Mach numbers being tested produce different Reynolds numbers beneath the boundary layer, and the injected Reynolds number varies. However, it is also important to establish the grid independence of the mesh, and this could affect meeting the minimum mesh density criteria. This is resolved by preserving the mesh density in the capsule near-field section and changing the densities of the fore and aft far-field sections. The sizing of the mesh near the edges of the capsule can be seen clearly in Figure 9, which shows that the minimum sizing of the grid is on the order of a centimeter about the curved edges. Though the use of multiple meshing zones provides some advantages, there are some concerns it provides as well. Because the meshing sizing is not consistent across the different zones and different element types are used, meshing quality across boundaries is compromised. In addition to this, the mesh size must inflate in the fore and aft far-field regions because they are structured and the number of divisions in the grid must be preserved from the interior of the mesh to the exterior of the mesh. However, the unstructured mesh isn't restricted in this way and its density is nearly constant across the entirety of the near-

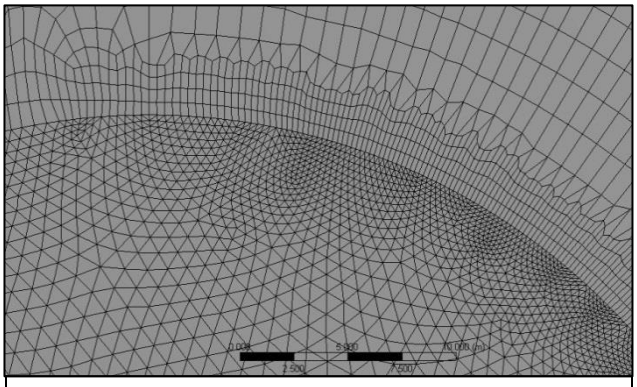

Figure 10: Unstructured mesh at the boundary of the aft far-field meshing zone and capsule near-field zone.

field domain. Because of this, the boundaries of the meshing zones have elements that are elongated, but their aspect ratio is below four, so that they still maintain the computational quality necessary to resolve the flow. Furthermore, the areas in which the mesh quality is diminished are also far away from important features of the flow, like the bow shock and wake behind the capsule. The mesh presented in this paper has a total of some 73,000 cells, the majority of which are in the near-field zone of the mesh.

Chapter 3.2: Boundary Conditions

As with every system of partial differential equations, the boundary conditions greatly influence the conditions within the domain. For this reason, the treatment of such boundary conditions is of vast importance to the accuracy of the solution. The problem considered in this paper is one where the treatment of both the momentum of the flow and the thermal conditions of the flow are greatly important. Furthermore, the fact that the model is axisymmetric means that the boundary conditions are also influenced by the placement of the symmetry axis. As seen in Figure 7, the edges of the fore and aft far-field mesh zones that are furthest away from the capsule geometry are treated as a pressure far field. At these boundaries the Mach number is defined based on the simulation being run, ranging from 5 to 10 in whole numbers. The gauge pressure at this boundary is defined as being zero, because the pressure about the far field should be treated as the defined operational pressure. Because the Mach number is defined directly and the pressure and temperature are defined at the boundaries in lieu of density, the Reynolds number needs to be calculated indirectly.

The temperature at the boundary is also important to the formulation of the Eckert number, so it is set to be 300 Kelvin. This means that the operating pressure must be allowed to

vary in order to set the Reynolds number, which may become problematic at low Reynolds numbers and high Mach numbers due to the low pressures needed to model such flows. This runs the risk of the flow being rarified, and Knudsen effects becoming dominant in the flow because the mean free path of the molecules is on the order of the length scale of the geometry in consideration. Therefore, it is critical to make sure that the Knudsen number of the flow is low enough that such effects can be ignored, otherwise the assumption of continuity in the flow is inaccurate, and the governing equations of the fluid flow are invalid. Even the boundary conditions, like the assumptions made about the no slip condition and therefore the conduction at the boundaries, become invalid in such flows, since the molecules in a given flow can still move near the walls of a geometry, but their averaged motion in bulk is a net zero velocity when the flow is considered continuous. This would be problematic for the model considered, and would require the use of a stochastic model as opposed to one based around differential equations. Furthermore, molecular diffusion in rarefied flows is not nearly as well understood as in continuous mediums, so the fact that the flow may be treated as a continuous fluid means that the diffusion can be modeled without needing to derive a novel method. For this study, the most critical test point in the flow is when the Mach number is set to 10 and the Reynolds number to 10,000, which is where the flow is most likely to become rarified. The calculation of the Knudsen number can be obtained using the Reynolds number and Mach number using the following relation:

$$73)\ Knudsen\ number\ \equiv Kn = \frac{Ma}{Re}\sqrt{\frac{\gamma\pi}{2}} = \frac{10}{10{,}000}\sqrt{\frac{1.4\pi}{2}} = 0.001483\ \ll\ 1$$

This means that the Knudsen number of the flow is not high enough for it to be considered free molecular flow, and the assumption of continuity of the flow is still valid.

The far-field boundary conditions are also defined in terms of the species concentrations since the problem in consideration also analyses mass transport. The species conditions at the far field boundary are defined as being 23% Oxygen by mass and 77% Nitrogen by mass, similar to the composition of sea level air in the standard atmosphere. During descent the actual composition of the atmosphere will not necessarily be the same as that of sea level, but the compositions of the atmosphere through the majority of the atmosphere where deceleration and heating occur have a very similar composition. Turbulence parameters must also be defined in the far field, since the k-epsilon turbulence model is being utilized in this paper to model the effects of turbulence on the flow and the heat transfer experienced. To do this, the hydraulic diameter of the geometry and the intensity of the turbulence are defined by the user as five meters and 5% respectively. All other parameters are left as their default values in Fluent 16.1. In addition to the far-field boundary conditions, there are also the boundary conditions at the walls of the capsule and the injection nozzle. The walls of the capsule encompass all the interior curves of the mesh with the exception of the foremost curve, which acts as the nozzle. These curves are split and defined separately for the sake of post processing considerations, into three regions known as the capsule wall, side wall, and back wall respectively, but the boundary conditions applied to all of them are the same. When modeling the flow without injection, the nozzle is treated as a wall and the same boundary conditions are applied. Each of the walls is treated with a no-slip condition, so that the velocity at the boundary is zero. In addition to this, the walls are treated as isothermal boundaries set at 300 Kelvin. These walls are given a thickness of one centimeter and are modeled as being made of aluminum, which is a common material in aerospace engineering applications, and is fairly thermally conductive as well. Though this treatment of the walls does not display the transient behavior of the wall temperature

as a function of the total heat load over time, it does reveal the maximum rate at which heat enters the boundary, and allows the near wall temperature to be computed accurately. The temperature on the exterior of the wall tends not to exceed more than a few degrees above the 300 Kelvin boundary condition due to the nature of the boundary condition itself. There are no species considerations at the walls to be considered, since none of the walls are porous, nor do they affect how the diffusivity is modeled. Defining these thermal boundary conditions is important to the modeling of the flow not only because they define the solution that arises, but because without such information, the post processing steps in CFD Post v16.1 that are required for this paper would not be possible.

When considering injected flow, the boundary conditions are changed significantly. The area of the capsule wall that is labeled as the nozzle becomes a pressure inlet, which has its back pressure and supersonic initial gauge pressure, defined according to the flow conditions at hand. These parameters are defined in such a manner that the flow in the nozzle, being 1.3 meters in diameter, is choked at approximately 498 meters per second, and the density is allowed to vary to meet the requirements of the flow. The species of the flow at this boundary condition is pure helium, at a temperature of 100 Kelvin, well above the vapor point of liquid helium. Having the flow eject at a constant velocity across the different injection cases for each Mach number studied has a benefit, namely that the Mach number of the injection is kept constant and does not need to be considered in the non-dimensional analysis as a result. This means that the Reynolds number may be varied by changing the density of the outgoing flow in the model, and thus the mass flow rate as well. The total and supersonic gauge pressures at the nozzle are selected in each case to keep the flow ejecting at a mass flow rate between one to four kilograms per second for the 10,000 Reynolds number cases and between 20 to 10 kilograms per second for

the 100,000 Reynolds number cases, although the results that have been obtained from this study suggest that these flow rates are perhaps excessive for the regime of the flow considered. Since the expansion ratio for helium to reach Mach 1 is approximately 2.05, the ratio between the total gauge pressure and the supersonic gauge pressure should be set as 2 for all cases with injected flow. The treatment of turbulence on this boundary condition is also similar to that of the pressure far field boundary condition discussed earlier in this section, but for this boundary the hydraulic diameter is set to 1.3 meters instead of five, but the turbulence intensity is similarly kept at 5%.

Chapter 3.2: Computational Setup

Even if the boundary conditions for this problem are defined carefully and in a meaningful way, the setup of the solution can still cause divergence to occur, and a non-physical solution to be obtained. Even having the solution bounded properly by computational limits on flow properties like the maximum and minimum pressures and temperatures that may occur does not help to ease the solution into a physically realizable solution without some additional effort. For this particular problem, these issues will begin to arise when the injection boundary conditions are added to the flow if proper treatment of them is not taken.

In general, for the flow to converge smoothly, the default limits on the solver must be revised to reflect the flow regimes high temperature environment and the low pressure environment. The limits must be set to 10,000 Kelvin for the maximum temperature, and 0.00025 Pascal for the lower bound on the pressure. Neither of these flow parameters will arise in the final solution of the case being run, but the temperature and pressure approach these limits while the solution is being solved, and they will act as indicators of whether or not the solution

will properly converge. All methods within the Solution Methods panel should be set to first order, to allow the solution to converge with greater accuracy. Though second order approximations are generally preferred, and this will cause the shock wave to be somewhat thick, the instability in convergence associated with second order approximations is not ideal, and would make the problem extremely difficult if chemical reactions were to be included as well. By default, the solution methods for the turbulence model will already be set to first order. The courant number and relaxation factors should also be revised for all calculations in order to maintain decent residuals during the calculations. The courant number should be set to 0.3 instead of 0.5, which adds time to the calculation itself, but allows for greater accuracy to be obtained. This can be neglected at the choice of the experimenter, but the accuracy lost will likely result in a poor solution. All turbulence under relaxation factors should be set to 0.8, but all others can remain unchanged. This choice may also be neglected, but it will actually result in a shorter convergence time if it is taken, since the error messages that fluent will generate will cause the solver to run slower if the turbulence reaches its limit within the solver. Calculations should ideally have a reporting interval of 25 iterations or lower. This adds some computation time, but it has the benefit of allowing you to disengage the solver more quickly if divergence becomes an issue. Above 25 iterations, the shape of the residuals is not immediately apparent, so it is more difficult to gauge if the solver is merely momentarily diverging or if it is a trend until some 200 iterations have passed, by which point well over a minute will have gone by. Each calculation requires at least 5000 iterations to be accurately converged when injection is not present. All species within the mixture panel should have all parameters set to kinetic theory, with the specific heat capacity of each gas being the only exception. For nitrogen and oxygen, these should both be set to piecewise polynomial expressions and the helium species should be

set to constant. The mixture itself should have its density set to ideal gas, its specific heat set to mixing law, and its thermal conductivity and viscosity set to ideal gas mixing law. The remainder of the fluid parameters may be set to kinetic theory. The use of the ideal gas law for the density is critical, since the far-field pressure boundary condition will not work without the use of the ideal gas law in the mixture. The pressure for each solution must be set within the operating conditions under the Define tab in fluent. The pressures should be set in accordance to Table 1 presented below:

FREE STREAM CONDITIONS										
MACH #	REYNOLDS	VELOCITY	STATIC PRESSURE	MACH #	REYNOLDS #	VELOCITY	STATIC PRESSURE	REYNOLDS #	VELOCITY	STATIC PRESSURE
5	10000	1739.527	1.703	5	100000	1739.527	17.03	1000000	1739.527	170.3
6		2087.4324	1.419	6		2087.4324	14.19		2087.4324	141.9
7		2435.3378	1.216	7		2435.3378	12.16		2435.3378	121.6
8		2783.2432	1.064	8		2783.2432	10.64		2783.2432	106.4
9		3131.1486	0.946	9		3131.1486	9.46		3131.1486	94.6
10		3479.054	0.852	10		3479.054	8.52		3479.054	85.2

Table 1: Free Stream Pressure conditions for Mach and Reynolds numbers studied in this paper. All pressures are in Pascals and velocities are in meters per second.

For the injected flows, the treatment of the setup is somewhat different. If the flow is initialized with the injection boundary condition, it will not converge properly and will exhibit reversed flow along the nozzle, and will hit both the high temperature and low pressure limits that are set in the solver. This is most likely because the flow is initialized from the pressure far field in all simulations, so that means the shock layer must grow out from the wall of the capsule doesn't form before the injection is present, and this means the total pressure of the fluid is still arbitrarily high near the wall, so it causes reversed flow to form, and this introduces additional computational errors that prevent the code from obtaining a physical solution. For this reason, it

is necessary to initialize injection problems first by treating the flow as if the nozzle is a wall with the same boundary conditions describe previously in this section. This initial run must be run to 5000 iterations to obtain a solution that will not immediately begin to introduce errors into the solver. This same procedure can be done with 2500 iterations for some cases, but the same problem may still arise. After the flow is initialized, the nozzle must be switched from a wall boundary condition to a nozzle with the conditions described above, and run for an additional 5000 iterations.

Each run of 5000 iterations takes approximately 20 to 30 minutes a piece, so this setup may take an hour to run. However, once the initial flow injection has been established, subsequent injection cases can be run from this point using only 2500 iterations. Since three injection cases are being looked at for each Mach and Reynolds number considered in the study, the total time elapsed for the injection cases is the same as the non-injection cases. It is extremely important to remember that once the boundary conditions are changed, the experimenter must not reinitialize the solver. Doing so will dump all data and will run the case as if the flow was being run from the first iteration with injection, and will not provide physically realizable results as a consequence. If done correctly, the first iteration should list that the flow is reversed and there will be a spike in the residuals after the boundary condition at the nozzle is changed, but the number of iterations will continue to increase beyond 5000. The flow reversal will quickly correct itself, and subsequent iterations should go smoothly without any errors or messages being displayed. It is also imperative that the temperature be reset in the thermal tab when switching from wall boundary conditions to injection boundary conditions. If this is not done, then the injection will occur at a speed roughly 890 meters per second, as opposed to 498 meters per second. The Mach number is still held at roughly one, but this will affect the Prandtl

number of the injected fluid, which will adversely affect the results that are obtained, and will also affect the shape of the wake being formed, since the Prandtl number has a strong effect on the wake flow thermal inversion of the model, as well as the shape of the recirculation bubble and the recompression shock.

CHAPTER 4: RESULTS

Chapter 4.1: Verification and Validation Measures

In order to determine the accuracy of the solutions that will be presented in this chapter, and subsequent ways in which the accuracy of the solutions may be improved, it is important to have some way to validate ones results in a meaningful way. This is particularly true of data obtained using computational methods, since experimentally obtained data has the luxury of generally not needing to confirm that assumptions about the physics of the problem are accurate, since all of the physics that would be present in the real world will still be present in the model. For this papers purposes, three different models have been used to look at the accuracy of the solution from the standpoint of the heat flux that occurs, namely, the Sutton-Graves model, which is widely used, the Detra-Hidalgo model [Aerothermal Analysis of a Sample-Return Reentry Capsule], and a method provided in John D. Andersons book *"Introduction to Flight 7th Ed."*. These methods are shown in the order that they are listed below:

74) $\dot{q} = 1.78 \times 10^{-4} \sqrt{\frac{\rho_\infty}{R_n}} V_\infty^3 , \qquad in \ \frac{W}{m^2}$

75) $\dot{q} = 5.16 \times 10^{-5} \sqrt{\frac{\rho_\infty}{R_n}} V_\infty^{3.15}, \qquad in \ \frac{W}{m^2}$

76) $\dot{q} = \frac{1}{4} \rho_\infty V_\infty^3 \left(\frac{C_f}{C_D}\right), \qquad where \ \frac{C_f}{C_D} \approx 0.05$

Results from this study show similarities to the above described models in terms of their overall shape, but the heat fluxes of the computational results are for the most part larger than those seen in either the Sutton-Graves or Detra-Hidalgo models. This is most likely because these quasi-empirical models are fitted against historical data, which means they capture the effects of

chemical dissociation within them, as well as a more accurate picture of atmospheric gas composition. In general, this studies computational results tend to show heat fluxes that are roughly twice that of the Sutton-Graves or Detra-Hidalgo models. The model presented by John D. Anderson is less agreeable at low Reynolds numbers, but is much closer to the computational results at higher Reynolds numbers. However, since both the Sutton-Graves and Detra-Hidalgo models are better established in literature, they should be taken as the primary guidelines to the accuracy of this solution to real world examples. Such inaccuracies were anticipated at the outset of this study, whose purpose was to qualitatively capture the physics occurring, and to provide a conservative estimate of the heating profile that would be encountered. Though the heat fluxes in the computational data are much larger, they tend to consistently be about twice that of the Sutton-Graves and Detra-Hidalgo models, and follow along the same trend lines. This becomes more apparent as the Reynolds number of the flow is increased. Another reason that the heat flux of the computational data is higher in general than the semi-empirical models is that the analysis is not transient, and the temperature of the walls of the capsule are assumed to be set at a constant 300 K. This means the heat flux will be

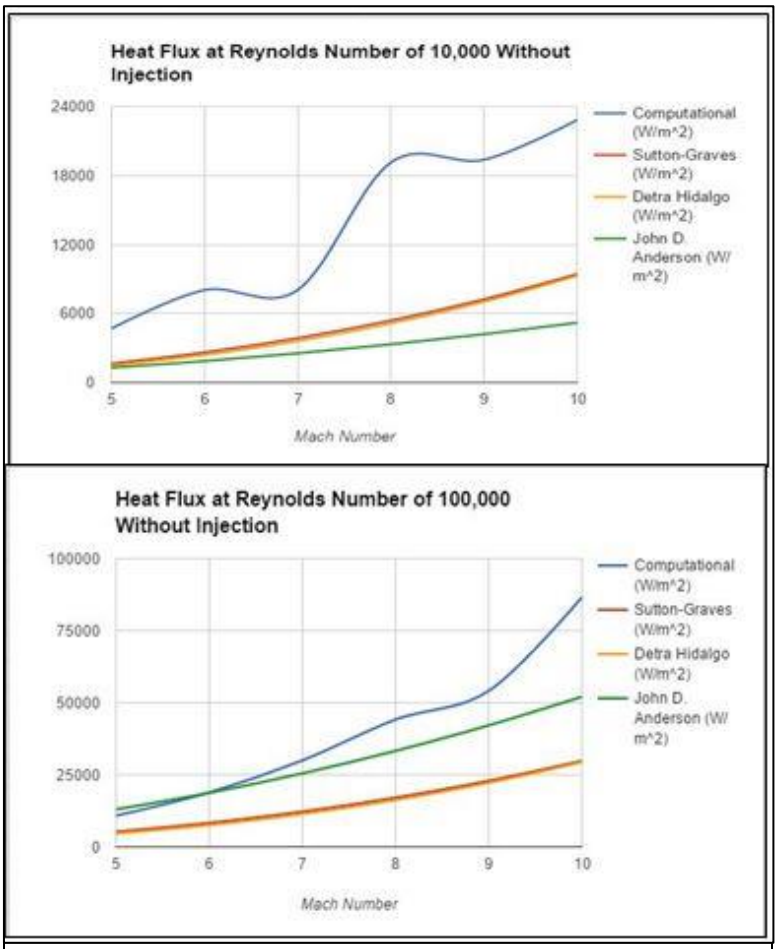

Figure 11: Comparison of heat flux data at Reynolds numbers of 10,000 and 100,000 with quasi empirical models.

arbitrarily high, since normal re-entry vehicles will have the surface of the vehicle heated to higher temperatures over time, which means less heat will enter the vehicle as a consequence. A tabulated version of this data set can be found in Appendix A, along with data for higher Reynolds numbers as well.

Table 2: Residuals for non-injecting flow at a Reynolds number of 10000

RESIDUALS (NO INJECTION, RE 10000)								
MACH #	Continuity	x-velocity	y-velocity	energy	k	epsilon	O2	N2
5	4.12E-02	6.57E-03	1.85E-02	1.44E-02	1.00E-04	5.96E-04	3.53E+12	3.58E+12
6	5.85E-02	8.22E-03	2.49E-02	1.99E-02	1.12E-04	3.82E-04	3.59E+12	3.58E+12
7	7.25E-02	1.15E-02	2.93E-02	2.41E-02	1.23E-04	2.34E-04	1.33E+12	1.32E+12
8	4.43E-02	3.34E-02	1.59E-02	9.89E-03	1.22E-04	3.91E-04	1.45E+12	1.59E+12
9	3.28E-02	4.23E-03	1.23E-02	9.55E-03	1.06E-04	1.28E-04	1.91E+12	1.88E+12
10	1.87E-02	1.88E-03	5.93E-03	5.01E-03	8.53E-05	1.13E-04	3.08E+13	3.07E+13

Other important considerations to the validation of this model include its computational residuals, which show the quality of the convergence of the model, and its Y+ values along the boundaries, which determine how well the turbulent boundary layer has been resolved. For both the injecting and non-injecting cases the residuals tend to hover around 0.01 for all quantities of importance with the exception of the diffusion of nitrogen and oxygen in the medium, whose residuals tend to be in the range of 1E+13. However, this is most likely caused by diffusion conditions at the outlet of the pressure far field, and the treatment of the diffusion of species near the capsule walls and in

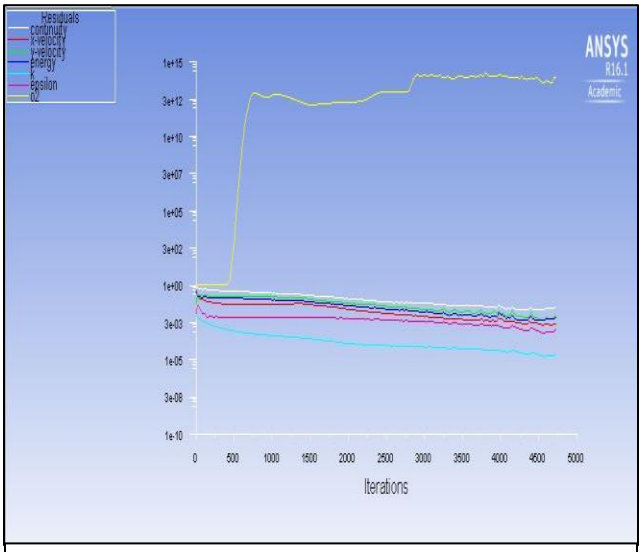

Figure 12: Residuals for flow at Mach 5 with a Reynolds number of 100,000, with no flow injection

the immediate wake of the flow is still physically accurate for the purposes of the simulation. More data regarding the residuals of the various simulations can be found in Appendix B of this paper.

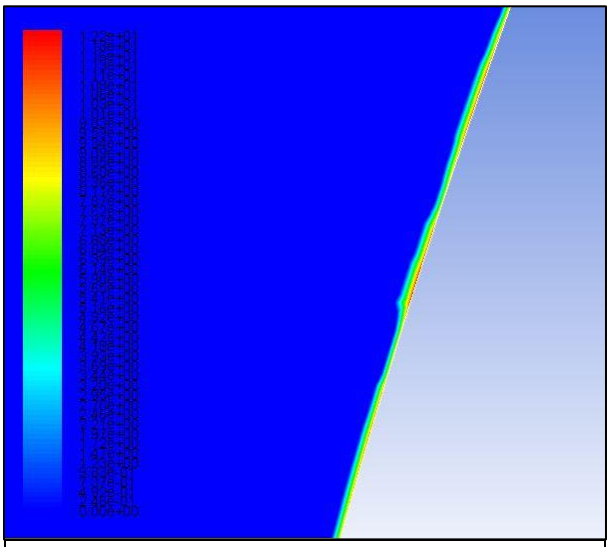

Figure 13: Y+ values at Mach 10 with a Reynolds number of 1,000,000, without injection.

For most of the flows considered in this study, the maximum Y+ values near the walls are within acceptable bounds, particularly for the non-injecting flow cases. Though some do exceed 11 at points, the Y+ value never exceeds 20 in the non-injecting flows. As the Reynolds number is increased, so too does the peak Y+ value exhibited. Injecting flow has a similar, but much more pronounced effect on the Y+ values, in some cases causing them to become unacceptably high, particularly for cases where the free stream Reynolds number is 1,000,000. This is most likely caused by the fact that the injected fluid is much colder, and thus less viscous, which causes the Y+ value to be much higher. However, the fight regime that the Orion Capsule would be in does not actually reach Reynolds numbers this high, as Figure 14 shows. In fact, for the Mach numbers considered in this study, the Reynolds number is nearly constant, during its hypersonic trajectory, staying at around 25,000 for the majority of its descent.

Figure 14: Flight profile of Orion Capsule in terms of Reynolds and Mach numbers

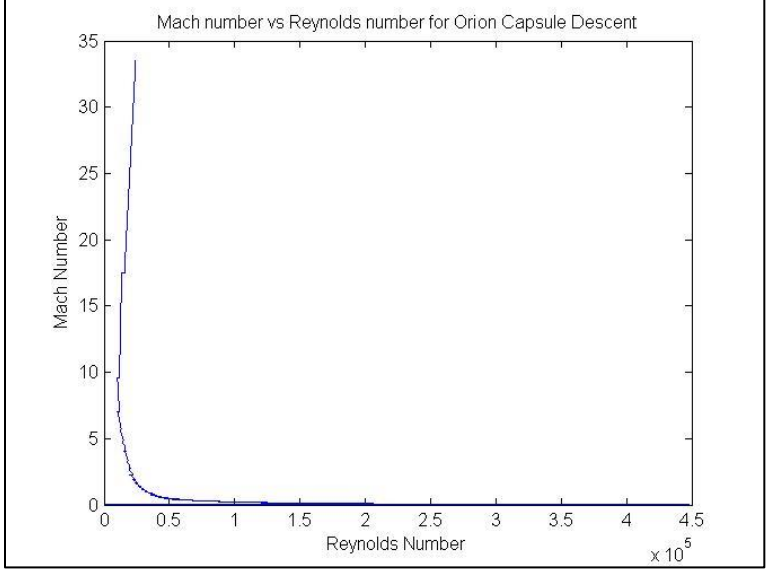

Nevertheless, future endeavors to study hypersonic flights of this capsule with Reynolds numbers of 1,000,000 or higher should take this into consideration and refine the sizing of the cells nearest the boundary of the geometry beyond what this study has done. If the sizing of cells closest to the wall were to be increased by an order of magnitude, then this would prove more than sufficient to resolve the boundary layer completely.

Qualitatively, the phenomena that are normally present in hypersonic flows about re-entry vehicles appear to be present in the results presented here. Besides the bow shock, the simulations also capture phenomena such as the recompression shock wave, expansion waves about the lip of the capsule, and a recirculation bubble at the base of the capsule due to viscous effects, which can be seen in Figure 15 to the right.

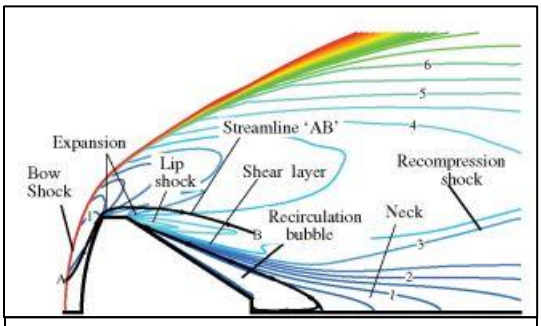

Figure 15: Flow characteristics for FIRE II reentry vehicle at Mach 13 [Hypersonic Turbulent Flow Simulation of FIRE II]

In addition to this, the presence of wake flow thermal inversion can be noted in simulations conducted at higher Reynolds numbers, which is consistent with previous research done on the topic of wake flow thermal inversion [Similarity Laws of Re-Entry Aerodynamics – Analysis of Reverse Flow Shock and Wake Flow Thermal Inversion Phenomena]. These features can be seen clearly in Figure 16, which exhibits wake flow thermal inversion in the recirculation bubble in the portion of the wake immediately following the capsule. However, when viewing the thermal contours of the flow at the same Mach number, but at a lower Reynolds number,

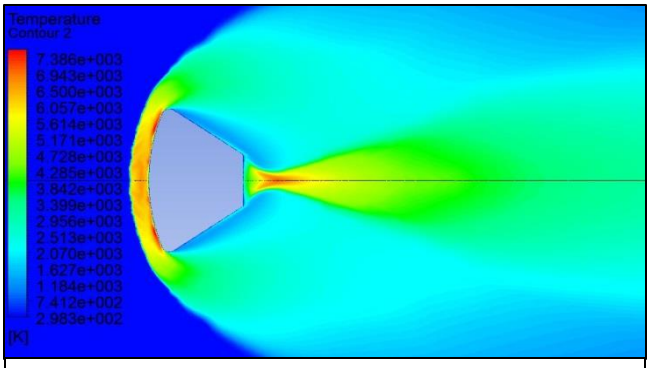

Figure 16: Static temperature contours at Mach 10 with a Reynolds number of 1,000,000

this phenomenon is not present.

To the right is Figure 17, which displays temperature contours at the same Mach number as Figure 16, but at a Reynolds number of 10,000 instead of 1,000,000. There is a noticeable difference in the thermal profiles of the two. Besides the standoff distance of the bow shock in the low Reynolds number case being significantly smaller, the temperature in the recirculation bubble and converging shock are significantly lower. Both profiles reach a temperature of around 5500 K in the region immediately behind the bow shock, but the high Reynolds number case reaches a temperature of nearly 7400 K near the neck of the flow before the converging shocks, while the low Reynolds number case has temperatures below 3000 K in this same region of the flow. This agrees with observations in Balange and Boyce's 2007 paper on the topic, that states that the phenomenon occurs when the Reynolds number of the flow is high, and when the Prandtl number of the flow is near unity.

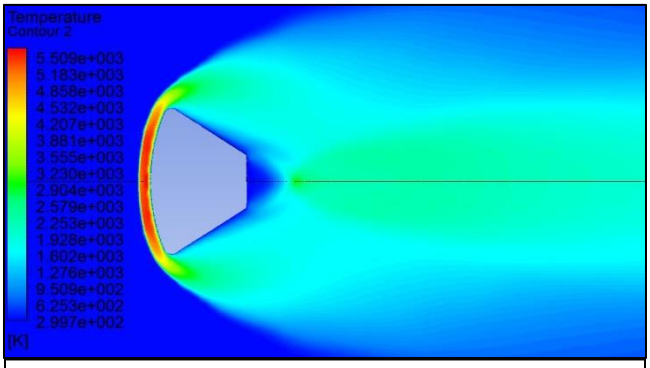

Figure 17: Static temperature contours at Mach 10 with a Reynolds number of 10,000

Chapter 4.2: Injections Effect on Drag and Pressure Distributions

The effect that injection of gaseous helium has on the drag experienced by the Orion capsule is counterintuitive. One would normally expect that the momentum of a high speed jet being ejected in the direction opposite of the freestream air would increase the drag of a vehicle. The jet itself has anywhere between 100 to 10,000 Newtons of thrust, depending on the Reynolds number of the flow. However, the drag of the vehicle is not increase, but actually significantly reduced by the use of the fluid injecting cooling system, with the drag coefficient being reduced

from an average of 2.05 in non-injecting cases, to an average of 0.96 with the injection. The drag estimates for the capsule without injection are consistent with NASA Langley's own estimates of the capsule's drag coefficient of 1.96 when at a 0 degree angle of attack, so it is unlikely that computational errors are the cause of this dramatic shift in the drag [Orion Aerodynamics for Hypersonic Free Molecular to Continuum Conditions]. The drag coefficient for cases with injection is relatively constant, and is not strongly influenced by either the Reynolds number of the injection or the Reynolds number of the free stream flow, nor the Mach number. It does begin to increase with the increase of the injected Reynolds number beyond a certain point, but the drag coefficient is still nearly half of what it is without injection. This can be seen in Figure 18 to the left, which shows that the drag coefficient drops sharply before gradually rising again after a certain injection Reynolds number, the value of which increases as the Mach number increases, and at a slope that decreases as the Mach number increases. This reduction in drag may be attributable to three different effects, each of which affect the wave drag, pressure drag, and viscous drag respectively. The first of these effects is the effect that the secondary shocks beneath the main bow shock have on the total pressure that reaches the capsule walls.

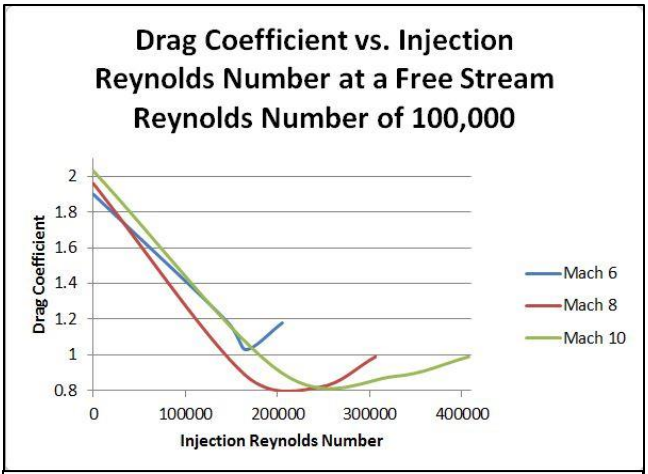

Figure 18: Drag coefficient vs injection Reynolds number for different Mach numbers at a Reynolds number of 100,000

Because the injected flow is coming out at a speed that is locally sonic, it experiences a normal shock upstream of the flow, which interacts with the bow shock in two ways. It increases the distance that the bow shock stands off from the face of the capsule considerably, particularly at lower Reynolds numbers, and it lowers the maximum pressure behind the bow shock as well. This is likely because the secondary shocks beneath the main bow shock cause a larger loss of total pressure, which reduces the drag on the capsule. In addition to this, the increased standoff distance of the bow shock causes more of the shock to be oblique, which means fluid on a larger amount of the surface of the vehicle will not be stagnant, and instead will flow around the vehicle. Both of these effects can be seen in Figure 19 above. The non-injecting flow above has pressure of 114 Pascals over the majority of its front, while the fluid surrounding the injected flow case below it has a maximum pressure of 50 Pascals on the surface of the capsule, and the maximum pressure behind the bow shock has been reduced to 100 Pascals. Additional effects that the gaseous helium has on the drag have to do with both its temperature and its properties as a gas. Because helium has a lower molecular weight than the principal species present in air, it has a lower density as well. Density of a flow is directly proportional to the dynamic pressure of the flow, as well as its static pressure. However, helium also has a much higher gas constant than air as a result of its low molecular weight as well, but the fact that it's stagnation temperature is a mere

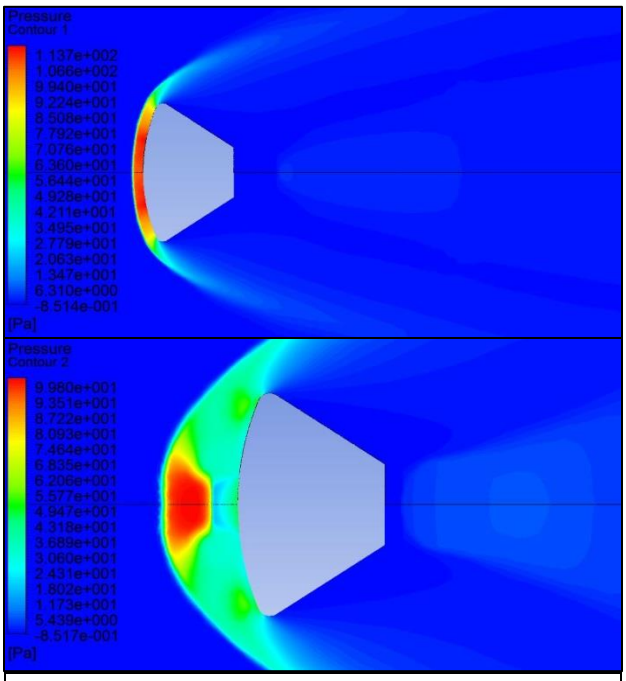

Figure 19: Pressure distributions at Mach 10 with a free stream Reynolds number of 10,000 for a non-injecting case (above) and an injecting case (below)

100 K, as opposed to thousands of Kelvin of the free stream, means the stagnation pressure of the helium is significantly lower than that of the free stream air. When the concentration of cold gaseous helium near the walls is increased, the pressure will go down. This in turn decreases the drag felt by the vehicle due to pressure on its surface. The last effect, which mainly effects the viscous or parasitic drag, is due to the effect of Sutherlands law. Colder gasses are naturally less viscous than hotter ones, with the temperature of the gas to the power of 1.5 being proportional to the viscosity of the gas itself. With the proper amount of injected fluid into the flow, the temperature of the surface of the capsule can be brought to temperatures below that of the free stream and capsule walls. This would drastically reduce the effect of viscosity around the capsule, reducing a portion of the drag as well as delay separation of the flow, by lowering momentum losses in the fluid near the walls. In Figure 20 above, the distribution of helium by mass fraction is shown. The helium is in higher concentration closest to the capsule walls, which would allow it to lower the viscosity of the fluid surrounding the walls by cooling them. However, the viscous drag for a blunt body such as this one are a low fraction of the total drag the vehicle experiences, so the effect the injection has on the bow shock and fluid immediately behind it is most likely the dominant effect that is reducing the drag. These results agree with those found in a similar study that was presented at the 42nd AIAA Joint Propulsion Conference and Exhibit [Effect of Counterflow Jet on a Supersonic Reentry Capsule]

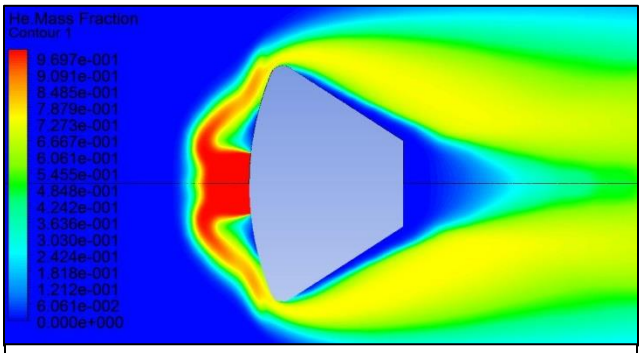

Figure 20: Helium mass fraction distribution at Mach 10 with a free stream Reynolds number of 10,000.

Chapter 4.3: Injections Effect on Heating and Temperature

Like the systems effect on the drag of the vehicle, the effect of the injected flow also has a somewhat counterintuitive effect on the heating and temperature distribution of the vehicles surface. While the injection does in general dramatically limit the amount of heat flux to the surface, and keeps the maximum temperature at the surface of the capsule well below 1000 K, using a smaller amount of injected fluid tends to cool the capsule more effectively and to lower temperatures than does a larger amount of injected fluid. This can be seen clearly in Figure 21 to the left. Both the maximum wall temperature and the heat flux initially drop up to a certain injection Reynolds number, but when the amount of injected fluid is increased beyond a certain point, the temperature and heat flux rise. Though counterintuitive, there is a probable explanation to why this is

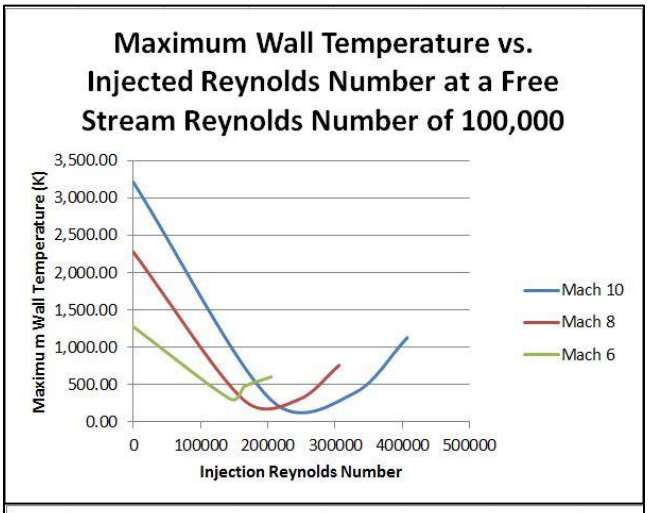

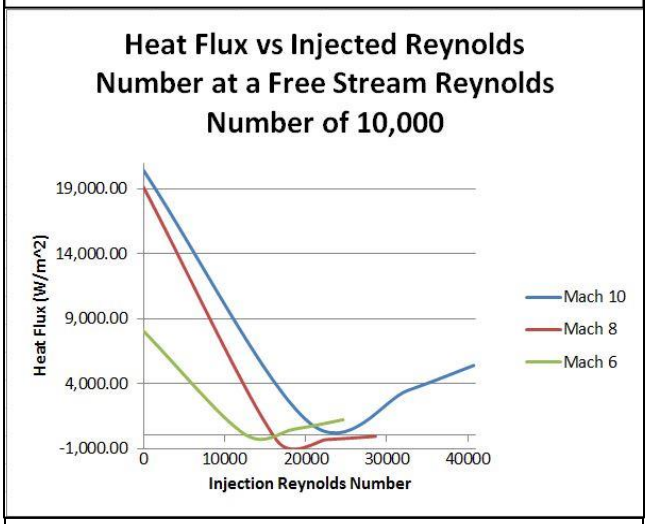

Figure 21: Temperature and heat flux vs injection Reynolds number for free stream Reynolds numbers of 100,000 and 10,000 respectively

occurring. The injection of the flow at higher Reynolds numbers carries a larger amount of momentum in the fluid, which in turn allows the helium jet to extend further from the wall of the

Figure 22: Velocity contours (left) and helium mass fraction contours (right) for a low Reynolds number injection case (top) and a high Reynolds number injection case (bottom) for Mach 8 with a free stream Reynolds number of 10,000

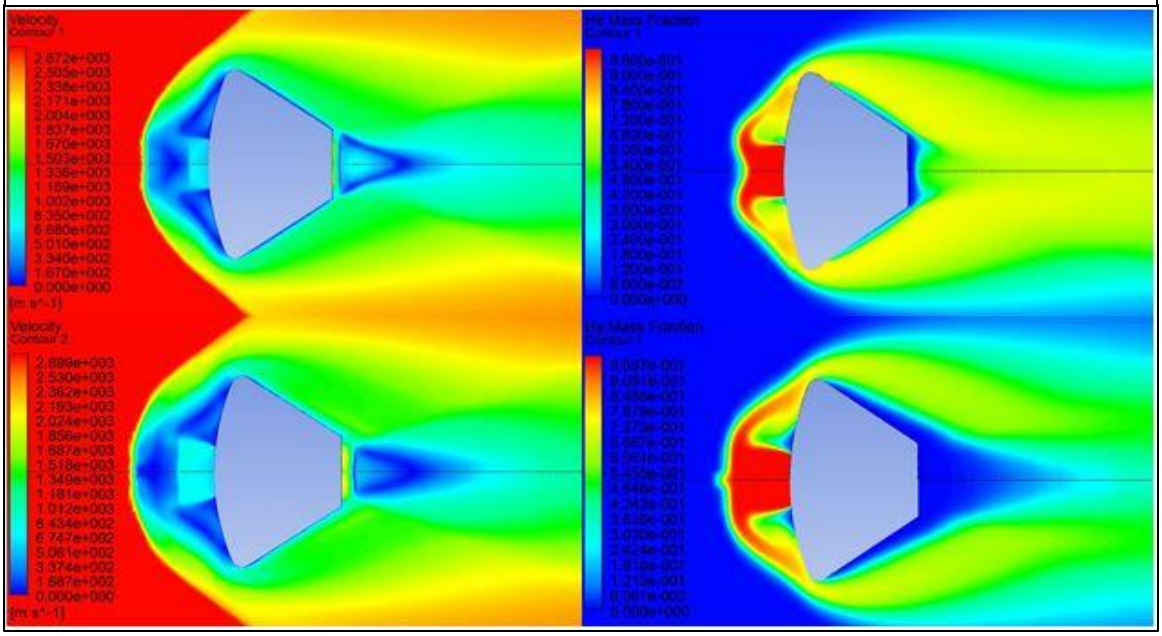

capsule. This allows the incoming flow to carry more of the cool gas past the walls of the capsule, without it ever being able to impinge upon the surface before being diffused with hot air. Figure 22 below shows velocity contours (left) and helium mass fraction contours (right) for both a low injections Reynolds number case (top) and a high Reynolds number injection case (bottom). Comparing the two cases, it is clear that the further the helium jet gets from the wall of the capsule before encountering a normal shock, the further away the shroud of back flowing cold gas will be from the center of the capsule before impinging on the surface. In the high injection Reynolds number case, there is a portion of the wall that almost none of the injected fluid actually interacts with about the center of the capsule wall, whereas the low injection Reynolds number case envelops nearly the entire capsule, including the wake of the capsule. However, this result is obtained for a flow that is chocked, and a denser flow with the same

Reynolds number could be obtained by varying the Mach number of the injected flow instead. This may have a dramatically different effect, since the shock interactions that are present in this study would not exist if the flow were not locally sonic. Alternately, the use of multiple nozzles may also reduce this effect, since a more even distribution of the injection gas can be achieved if multiple distributed nozzles are used as opposed to a central one.

These results are particularly encouraging, since they suggest that not only can the fluid injection cooling system keep temperatures and heat fluxes on the surface of the capsule to within tolerable levels, but that even less propellant may potentially be used to achieve this result than was previously anticipated. Even for a capsule made from less exotic materials, such as Aluminum 6061 or Steel 1045, the level of cooling provided by the fluid injecting cooling system proves adequate for the heat loads these materials can tolerate at high Mach numbers.

Chapter 4.4: Content of Appendixes

The remainder of the results in this paper may be found in Appendixes A and B. Appendix A contains tabulated data that has been acquired over the course of this study, whereas Appendix B contains contours of temperature, pressure, velocity, and helium mass fractions for the cases considered, as well as plots of the residuals and contours of Y+ values near critical locations along the capsule walls. Appendix C contains scripts and programs that were implemented during the course of this study.

CHAPTER 5: CONCLUSIONS

Chapter 5.1: Implications and Applications

The results of this study show that the use of fluid injection cooling systems could be a feasible method of heat dissipation up to Mach 10 for the Orion Crew Module. Given the rate of propellant consumption required for cooling, an estimated mass of 600 kg of helium could provide heat shielding to the craft for up to 33 minutes while traveling at Mach 10 along its trajectory using current estimates, while using a relatively conservative approximation of the heat loads encountered. At the very least, this data shows that such cooling systems would be an excellent complement to extend the mission capabilities of thermal soak heat shields that are used currently, if not outright replace them and ablative heat shields altogether. This result shows that the feasibility of this concept is high enough that it merits further study in flight regimes with higher Mach numbers to show whether or not it can still provide adequate cooling with sufficiently low amounts of mass. As it stands currently, there is some reason to believe that a fluid injection cooling system may be capable of shielding the capsule sufficiently at much higher Mach numbers while reducing the total amount of mass required for heat shielding compared to conventional systems. If nothing else, the fact that such a system could potentially allow for the use of more common materials in construction of the heat shield, like Steel 1045, or other metallic compounds, makes it worth considering. This, coupled with the reusability of such a system, and the ability to control the amount of injected fluid being used gives the system enough novelty that it could still be a best option even if the cumulative mass of the system exceeds that of current heat shields, simply because there will be mission profiles where precise

control of aerodynamic heating in real time without human intervention will be necessary, or where the ability to reliably reuse a heat shield is a system requirement.

In addition to applications studied in this paper, the drag reducing effects of the fluid injecting cooling system may have application in other types of hypersonic vehicles, such as air breathing scramjet based missiles and aircraft. At a flight speed of Mach 10, with a 30 minute endurance, a scramjet based vehicle could potentially cover a distance of over 6000 kilometers while flying through the upper atmosphere, all while using a smaller propulsion system and less fuel because of the reduced drag the cooling system offers. For such vehicles, other gasses like nitrogen may be preferable, since they are significantly cheaper than helium, and mass constraints are less severe than those for reentry vehicles. Cold gaseous oxygen could also potentially be used in a fluid injection cooling system for the scramjet itself, which would have the added benefit of precooling the flow, allowing it to be further compressed, and increasing the oxygen content of the incoming air, allowing combustion to occur at higher altitudes.

Chapter 5.2: Potential Improvements and Future Work

Though a great deal was learned over the course of this study regarding the feasibility of fluid injection cooling systems as an alternative to more conventional approaches to providing heat shielding, there is much more that still needs to be accomplished to mature this concept to a point where it may be applied. The scope of the data gathered in the study is miniscule compared to what it would need to be to accurately represent the entirety of the flow regime that could potentially be encountered by an object moving at hypersonic speeds, especially orbital speeds, and the accuracy of the solutions obtained is not high enough to warrant experimental modeling of the system. For this reason, future studies of this concept should seek to improve

the accuracy of the solution by increasing the density of the mesh to around 700,000 cells, or about an order of magnitude above what is currently used, add the effects of dissociation through modeling of the chemical reactions occurring, improve the residuals of the model by allowing for longer run times, and increasing the number of injected and free stream Reynolds numbers tested. Furthermore, the modeling of the flow was done using first order schemes, and further research into the topic should opt for second order schemes to avoid the presence of thick shock boundaries that are in this study, and to obtain more accurate solutions. In addition to this, a more accurate model of the injection nozzle may help to improve the accuracy of the results as well, along with modeling of any phase changes that may occur within the injection fluid. Helium is typically stored as a liquid, so at higher Mach numbers, modeling this phase change and heating from 4 K to 100 K will be necessary to accurately establish just how much injection fluid is required to cool the capsule effectively. However, the basic methodology established in this research will make such future endeavors significantly less labor intensive, and will allow them to be accomplished without much additional effort. These future studies should also make an effort to clarify questions that have been raised by this study, namely at what injection Reynolds number is optimum cooling achieved, what effect does the Mach number of the injected flow play, and how will a more distributed injection system affect the flow? Additional attention should be given to different species that could be used for injection, since only gaseous helium was considered in this study.

Most of the limitations of this study were imposed out of necessity due to time constraints and limited processing power available. If sufficient processing power was available to future studies of this topic, then there is no doubt that much more sophisticated and accurate representations of the flow and its characteristics could be obtained. However, the main

objective of this paper was accomplished in full. The potential feasibility of fluid injection cooling systems for use on hypersonic re-entry vehicles has been established, and conservative estimates as to their performance have been made, while capturing as much of the physics present in the flow as possible for the constraints given.

APPENDIX A: TABULATED DATA

1) Free Stream Conditions used at the far field boundary by Mach and Reynolds number

FREE STREAM CONDITIONS			
MACH #	REYNOLDS #	VELOCITY (m/s)	STATIC PRESSURE (N/m^2)
5	10000	1739.527	1.703
6		2087.4324	1.419
7		2435.3378	1.216
8		2783.2432	1.064
9		3131.1486	0.946
10		3479.054	0.852
MACH #	REYNOLDS #	VELOCITY (m/s)	STATIC PRESSURE (N/m^2)
5	100000	1739.527	17.03
6		2087.4324	14.19
7		2435.3378	12.16
8		2783.2432	10.64
9		3131.1486	9.46
10		3479.054	8.52
MACH #	REYNOLDS #	VELOCITY (m/s)	STATIC PRESSURE (N/m^2)
5	1000000	1739.527	170.3
6		2087.4324	141.9
7		2435.3378	121.6
8		2783.2432	106.4
9		3131.1486	94.6
10		3479.054	85.2

2) Residuals for non-injection cases by Mach and Reynolds number

RESIDUALS (NO INJECTION, RE 10000)								
MACH #	Continuity	x-velocity	y-velocity	energy	k	epsilon	O2	N2
5	4.12E-02	6.57E-03	1.85E-02	1.44E-02	1.00E-04	5.96E-04	3.53E+12	3.58E+12
6	5.85E-02	8.22E-03	2.49E-02	1.99E-02	1.12E-04	3.82E-04	3.59E+12	3.58E+12
7	7.25E-02	1.15E-02	2.93E-02	2.41E-02	1.23E-04	2.34E-04	1.33E+12	1.32E+12
8	4.43E-02	3.34E-02	1.59E-02	9.89E-03	1.22E-04	3.91E-04	1.45E+12	1.59E+12
9	3.28E-02	4.23E-03	1.23E-02	9.55E-03	1.06E-04	1.28E-04	1.91E+12	1.88E+12
10	1.87E-02	1.88E-03	5.93E-03	5.01E-03	8.53E-05	1.13E-04	3.08E+13	3.07E+13
RESIDUALS (NO INJECTION, RE 100000)								
MACH #	Continuity	x-velocity	y-velocity	energy	k	epsilon	O2	N2
5	2.89E-02	2.33E-03	6.62E-03	5.01E-03	1.33E-05	9.12E-04	3.89E+13	3.87E+13
6	2.78E-02	2.35E-03	6.17E-03	5.50E-03	1.09E-05	5.73E-04	2.60E+13	2.60E+13
7	2.27E-02	1.77E-03	4.40E-03	3.77E-03	8.37E-06	3.12E-04	2.16E+13	2.16E+13
8	1.31E-02	1.44E-03	3.69E-03	2.79E-03	8.91E-06	4.20E-04	1.32E+13	1.32E+13
9	2.21E-02	2.63E-03	5.88E-03	4.54E-03	2.33E-05	8.50E-04	6.74E+13	6.74E+13
10	2.40E-02	2.37E-03	4.86E-03	4.92E-03	1.52E-05	4.65E-04	2.28E+13	2.28E+13
RESIDUALS (NO INJECTION, RE 1000000)								
MACH #	Continuity	x-velocity	y-velocity	energy	k	epsilon	O2	N2
5	3.13E-02	4.83E-03	9.70E-03	1.41E-02	1.75E-05	1.69E-03	7.04E+13	7.04E+13
6	3.00E-02	5.12E-03	9.64E-03	1.16E-02	1.15E-05	1.03E-03	5.56E+13	5.56E+13
7	2.66E-02	3.35E-03	8.29E-03	1.15E-02	6.74E-06	4.90E-04	4.31E+13	4.31E+13
8	3.24E-02	3.84E-03	7.50E-03	1.30E-02	1.21E-05	1.08E-03	3.81E+13	3.81E+13
9	3.27E-02	2.73E-03	6.34E-03	1.25E-02	9.75E-06	9.68E-04	3.38E+13	3.38E+13
10	4.39E-02	3.15E-03	8.17E-03	1.54E-02	1.12E-05	1.11E-03	2.41E+13	2.41E+13

3) Results for non-injecting cases by Mach and Reynolds number

Flow Characteristics (NO INJECTION, RE 10000)									
MACH #	Heat Flux (W/m^2)	Ave. Wall Temperature (K)	Max. Wall Temperature (K)	Drag (N)	Ave. Nusselt #	Max. Nusselt #	Ave. Eckert #	Max. Eckert #	Drag Coefficient
5	4,703.80	521.8	722.6	1,095.80	4126	2165	13.57	7.12	1.86
6	8,053.00	685.46	863.08	1,581.30	4065	2782	11.25	7.7	2.24
7	8,055.70	668.88	952.81	1,419.90	4249	2401	16	9.04	1.72
8	19,149.00	988.13	1,213.79	2,491.70	5414	4077	11.2	8.43	2.65
9	19,384.00	996.98	1,361.30	2,255.80	5411	3553	14	9.19	2.13
10	22,843.00	1,077.90	1,414.88	2,439.40	5713	3986	15.48	10.8	2.07
Flow Characteristics (NO INJECTION, RE 100000)									
MACH #	Heat Flux (W/m^2)	Ave. Wall Temperature (K)	Max. Wall Temperature (K)	Drag (N)	Ave. Nusselt #	Max. Nusselt #	Ave. Eckert #	Max. Eckert #	Drag Coefficient
5	10,859.00	748.99	996.2	10,980.00	4705	3035	6.71	4.32	1.87
6	18,881.00	959.43	1,276.55	13,453.00	5570	3762	6.57	4.44	1.9
7	29,995.00	1,269.40	1,761.74	16,058.00	6020	3992	6.09	4.04	1.95
8	44,179.00	1,546.49	2,279.35	18,469.00	6895	4342	6.18	3.89	1.96
9	54,120.00	1,868.70	2,695.27	17,314.00	6712	4396	6.22	4.07	1.63
10	86,611.00	2,224.90	3,215.24	23,937.00	8754	5780	6.26	4.13	2.03
Flow Characteristics (NO INJECTION, RE 1000000)									
MACH #	Heat Flux (W/m^2)	Ave. Wall Temperature (K)	Max. Wall Temperature (K)	Drag (N)	Ave. Nusselt #	Max. Nusselt #	Ave. Eckert #	Max. Eckert #	Drag Coefficient
5	47,712.00	1,576.90	1,929.90	121,580.00	7270	5695	2.36	1.85	2.07
6	78,601.00	2,053.50	2,507.37	149,530.00	8721	6928	2.47	1.96	2.12
7	120,090.00	2,592.40	3,153.28	175,840.00	10192	8188	2.57	2.07	2.13
8	166,960.00	3,108.30	3,820.31	202,230.00	11567	9227	2.74	2.19	2.15
9	229,780.00	3,312.50	4,676.57	186,260.00	14840	10214	3.24	2.23	1.76
10	310,010.00	4,434.80	5,564.28	246,730.00	14587	11457	2.91	2.29	2.1

4) Validation of heat flux for non-injecting cases by Mach and Reynolds number

Average Heat flux at Re = 10,000				
MACH #	Computational (W/m^2)	Sutton-Graves (W/m^2)	Detra Hidalgo (W/m^2)	John D. Anderson (W/m^2)
5	4,703.80	1668.118803	1480.885065	1301.412673
6	8,053.00	2631.204418	2400.635102	1873.814163
7	8,055.70	3867.858239	3611.470977	2549.870154
8	19,149.00	5400.704503	5144.732381	3330.44265
9	19,384.00	7250.746762	7030.204989	4216.081867
10	22,843.00	9439.075028	9297.759599	5208.707446
Average Heat Flux at Re = 100,000				
MACH #	Computational (W/m^2)	Sutton-Graves (W/m^2)	Detra Hidalgo (W/m^2)	John D. Anderson (W/m^2)
5	10,859.00	5275.054826	4682.969758	13014.12673
6	18,881.00	8320.59895	7591.474752	18738.14163
7	29,995.00	12231.2417	11420.47399	25498.70154
8	44,179.00	17078.5272	16269.07228	33304.4265
9	54,120.00	22928.8745	22231.46018	42160.81867
10	86,611.00	29848.97609	29402.09747	52087.07446
Average Heat Flux at Re = 1,000,000				
MACH #	Computational (W/m^2)	Sutton-Graves (W/m^2)	Detra Hidalgo (W/m^2)	John D. Anderson (W/m^2)
5	47,712.00	16681.18803	14808.85065	130141.2673
6	78,601.00	26312.04418	24006.35102	187381.4163
7	120,090.00	38678.58239	36114.70977	254987.0154
8	166,960.00	54007.04503	51447.32381	333044.265
9	229,780.00	72507.46762	70302.04989	421608.1867
10	310,010.00	94390.75028	92977.59599	520870.7446

5) Pressure inlet boundary conditions for injecting cases by Reynolds and Mach number

MACH #	REYNOLDS #	Mass flow 1 (kg/s	Back Pressure (N/m^2)	Supersonic Gauge Pressure (N/m^2)
5	10000	0.2155	100	50
6		0.2573	120	60
7		0.299307	140	70
8		0.298996	140	70
9		0.319955	150	75
10		0.425766	200	100
MACH #	REYNOLDS #	Mass flow 1 (kg/s	Back Pressure (N/m^2)	Supersonic Gauge Pressure (N/m^2)
5	100000	2.155	1000	500
6		2.1447	1000	500
7		2.56554	1200	600
8		3.20048	1500	750
9		3.19357	1500	750
10		4.2578	2000	1000
MACH #	REYNOLDS #	Mass flow 2 (kg/s	Back Pressure (N/m^2)	Supersonic Gauge Pressure (N/m^2)
5	10000	0.1519	70	35
6		0.1937	90	45
7		0.1933	90	45
8		0.235392	110	55
9		0.256352	120	60
10		0.340963	160	80
MACH #	REYNOLDS #	Mass flow 2 (kg/s	Back Pressure (N/m^2)	Supersonic Gauge Pressure (N/m^2)
5	100000	1.519	700	350
6		1.72527	800	400
7		2.14516	1000	500
8		2.56605	1200	600
9		2.56364	1200	600
10		3.40963	1600	800
MACH #	REYNOLDS #	Mass flow 3 (kg/s	Back Pressure (N/m^2)	Supersonic Gauge Pressure (N/m^2)
5	10000	0.1095	50	25
6		0.1301	60	30
7		0.150903	70	35
8		0.171786	80	40
9		0.213949	100	50
10		0.213757	100	50
MACH #	REYNOLDS #	Mass flow 3 (kg/s	Back Pressure (N/m^2)	Supersonic Gauge Pressure (N/m^2)
5	100000	1.095	500	250
6		1.51304	700	350
7		1.72096	800	400
8		1.71802	800	400
9		2.13924	1000	500
10		2.13757	1000	500

6) Injecting flow results by Mach number and injection Reynolds number for a free stream Reynolds number of 10,000

MACH #	REYNOLDS #	Heat Flux (W/m^2)	Ave. Nusselt #	Injection Reynolds	Heat Flux (W/m^2)	Ave. Nusselt #	Injection Reynolds	Heat Flux (W/m^2)	Ave. Nusselt #	Injection Reynolds #
5	10000	708	2817	20614	209	2751	14530	-109	4493	10475
6		1218	2924	24613	489	2981	18529	117	2312	12445
7		-234	3377	28631	-233	3239	18491	-260	3250	14435
8		-69	6643	28601	-316	3309	22517	-373	3023	16433
9		1585	3872	30606	155	3040	24522	-115	2382	20466
10		5406	3864	40728	3482	3953	32616	992	3402	20447
MACH #	REYNOLDS #	Heat Flux (W/m^2)	Max. Nusselt #	Injection Reynolds	Heat Flux (W/m^2)	Max. Nusselt #	Injection Reynolds	Heat Flux (W/m^2)	Max. Nusselt #	Injection Reynolds #
5	10000	708	1643	20614	209	728	14530	-109	-461	10475
6		1218	1874	24613	489	1089	18529	117	242	12445
7		-234	-684	28631	-233	-2071	18491	-260	-6033	14435
8		-69	-119	28601	-316	-592	22517	-373	-977	16433
9		1585	1744	30606	155	188	24522	-115	-143	20466
10		5406	2328	40728	3482	2797	32616	992	819	20447
MACH #	REYNOLDS #	Ave. Wall Temperature (K)	Ave. Eckert #	Injection Reynolds	Ave. Wall Temperature (K)	Ave. Eckert #	Injection Reynolds	Ave. Wall Temperature (K)	Ave. Eckert #	Injection Reynolds #
5	10000	349	62	20614	315	204	14530	295	-633	10475
6		381	53	24613	332	136	18529	310	439	12445
7		287	-438	28631	286	-421	18491	284	-377	14435
8		298	-3812	28601	281	-415	22517	276	-320	16433
9		380	123	30606	310	982	24522	291	-1036	20466
10		572	44	40728	471	70	32616	357	211	20447
MACH #	REYNOLDS #	Max. Wall Temperature (K)	Max. Eckert #	Injection Reynolds	Max. Wall Temperature (K)	Max. Eckert #	Injection Reynolds	Max. Wall Temperature (K)	Max. Eckert #	Injection Reynolds #
5	10000	384	35.9	20614	356	54	14530	346	65	10475
6		426	34.28	24613	387	50	18529	394	46	12445
7		367	88.73	28631	322	269	18491	308	703	14435
8		413	68.1	28601	404	74	22517	374	104	16433
9		477	55.19	30606	461	61	24522	456	63	20466
10		752	26.65	40728	542	50	32616	536	51	20447
MACH #	REYNOLDS #	Drag (N)	Drag Coefficient	Injection Reynolds	Drag (N)	Drag Coefficient	Injection Reynolds	Drag (N)	Drag Coefficient	Injection Reynolds #
5	10000	536	0.91	20614	518	0.88	14530	638	1.08	10475
6		630	0.89	24613	618	0.88	18529	746	1.06	12445
7		717	0.87	28631	673	0.82	18491	582	0.71	14435
8		933	0.99	28601	875	0.93	22517	1004	1.07	16433
9		1070	1.01	30606	1080	1.02	24522	1466	1.38	20466
10		1089	0.92	40728	1084	0.92	32616	1065	0.9	20447

7) Injecting flow results by Mach number and injection Reynolds number for a free stream Reynolds number of 100,000

MACH #	REYNOLDS #	Heat Flux (W/m^2)	Ave. Nusselt #	Injection Reynolds #	Heat Flux (W/m^2)	Ave. Nusselt #	Injection Reynolds #	Heat Flux (W/m^2)	Ave. Nusselt #	Injection Reynolds #
5	100000	314	12529	206142	233	2753	145304	-275	1820	104745
6		1732	4343	205157	473	8924	165035	-112	1498	144734
7		872	11284	245413	-86	1660	205201	-156	2410	164623
8		878	15274	306150	-74	1417	245462	-348	1798	164342
9		2163	8193	305489	626	6829	245232	-184	1437	204635
10		5018	5226	407291	375	-38946	326157	-928	3882	204475
MACH #	REYNOLDS #	Heat Flux (W/m^2)	Max. Nusselt #	Injection Reynolds #	Heat Flux (W/m^2)	Max. Nusselt #	Injection Reynolds #	Heat Flux (W/m^2)	Max. Nusselt #	Injection Reynolds #
5	100000	314	456	206142	233.243	1049	145304	-275	-6544	104745
6		1732	1102	205157	473.013	522	165035	-112	-2787	144734
7		872	421	245413	-86.3014	-379	205201	-156	-16600	164623
8		878	370	306150	-73.5094	-147438	245462	-348	12387	164342
9		2163	640	305489	625.774	596	245232	-184	-729	204635
10		5018	1176	407291	374.74	957	326157	-928	110061	204475
MACH #	REYNOLDS #	Ave. Wall Temperature (K)	Ave. Eckert #	Injection Reynolds #	Ave. Wall Temperature (K)	Ave. Eckert #	Injection Reynolds #	Ave. Wall Temperature (K)	Ave. Eckert #	Injection Reynolds #
5	100000	305	617	206142	316	182.68	145304	271	-102	104745
6		378	56	205157	310	420.44	165035	285	-298	144734
7		315	392	245413	290	-583.47	205201	287	-469	164623
8		311	689	306150	290	-763.89	245462	262	-205	164342
9		351	190	305489	318	547.14	245232	275	-391	204635
10		487	64	407291	298	-6433.35	326157	253	-259	204475
MACH #	REYNOLDS #	Max. Wall Temperature (K)	Max. Eckert #	Injection Reynolds #	Max. Wall Temperature (K)	Max. Eckert #	Injection Reynolds #	Max. Wall Temperature (K)	Max. Eckert #	Injection Reynolds #
5	100000	434	22.47	206142	343	63.58	145304	308	368	104745
6		606	14.19	205157	476	24.59	165035	308	554	144734
7		703	14.63	245413	344	133.15	205201	302	3234	164623
8		761	16.71	306150	300	79460.45	245462	295	-1409	164342
9		957	14.84	305489	504	47.76	245232	349	198	204635
10		1130	14.5	407291	376	158.1	326157	298	-7339	204475
MACH #	REYNOLDS #	Drag (N)	Drag Coefficient	Injection Reynolds #	Drag (N)	Drag Coefficient	Injection Reynolds #	Drag (N)	Drag Coefficient	Injection Reynolds #
5	100000	5906	1	206142	5991	1.02	145304	5520	0.94	104745
6		8362	1.18	205157	7264	1.03	165035	8376	1.19	144734
7		8780	1.07	245413	7949	0.96	205201	10355	1.26	164623
8		9287	0.99	306150	7766	0.82	245462	8428	0.89	164342
9		11282	1.06	305489	11702	1.1	245232	12997	1.23	204635
10		11628	0.99	407291	10347	0.88	326157	10557	0.9	204475

APPENDIX C: MATLAB SCRIPTS

1.) Script for calculating capsule trajectory data

```
function [ Mach, Re, V ] = TRAJECTORYCALC(Vinf,phi)
%TRAJECTORYCALC: Will give you the trajectory of a body given
%   Function for calculating the trajectory of a projectile upon entering
%   the atmosphere of a given gravitational body and atmosphere.  The
%   coefficient of drag is assumed to be 1 as a blunt body approximation.
%   The drag coefficient's dependence on Reynolds number and Mach number
%   shall be shown in later versions shall as better data for the craft
%   becomes available.
h = .001;
Cd = 1;
D = 5;
S = 3.1415*(D/2)^2;
m = 7891;
g = 9.81;
R = 287.058;
Alti = [0:2000:86000];
Temp = [288.1 275.2 262.2 249.2 236.2 223.3 216.6 216.6 216.6 216.6 216.6
218.6 220.6 222.5 224.5 226.5 228.5 233.7 239.3 244.8 250.4 255.9 261.4 266.9
270.6 270.6 269.0 263.5 258.0 252.5 247.0 241.5 236.0 230.5 225.1 219.6 214.3
210.3 206.4 202.5 198.6 194.7 190.8 186.9];
Dens = [1.225 1.007 .8193 .6601 .5258 .4135 .3119 .2279 .1665 .1216 .08891
.06451 .04694 .03426 .02508 .01841 .01355 .009887 .007257 .005366 .003995
.002995 .002259 .001714 .001317 .001027 .0008055 .0006389 .0005044 .0003962
.0003096 .0002407 .0001860 .0001429 .0001091 .00008281 .00006236 .00004637
.00003430 .00002523 .00001845 .00001341 .000009690 .000006955];
Visc = [17.89 17.26 16.61 15.95 15.27 14.58 14.22 14.22 14.22 14.22 14.22
14.32 14.43 14.54 14.65 14.75 14.86 15.14 15.43 15.72 16.01 16.29 16.57 16.85
17.04 17.04 16.96 16.68 16.40 16.12 15.84 15.55 15.26 14.97 14.67 14.38 14.08
13.87 13.65 13.43 13.21 12.98 12.76 12.53]*10^-6;
xo = 0;
yo = 85000
vyo = -Vinf*sind(phi)
vxo = Vinf*cosd(phi)
to = 0;
t = zeros([1 2000000]);
t(1) = to;
X = zeros([1 2000000]);
X(1) = xo;
Y = zeros([1 2000000]);
Y(1) = yo;
Vx = zeros([1 2000000]);
Vx(1) = vxo;
Vy = zeros([1 2000000]);
Vy(1) = vyo;
V = zeros([1 2000000]);
V(1) = (vxo^2 + vyo^2)^(0.5);
Mach = zeros([1 2000000]);
Re = zeros([1 2000000]);
for count = 1:1999999;
    m = floor(Y(count)/2000);
    n = ceil(Y(count)/2000);
    k = (Y(count)- Alti(m))/(Alti(n)-Alti(m));
    tempcalc = Temp(m) + k*(Temp(n)-Temp(m));
    denscalc = Dens(m) + k*(Dens(n)-Dens(m));
```

```
    visccalc = Visc(m) + k*(Visc(n)-Visc(m));
    Mach(count) = V(count)/(R*tempcalc)^.5;
    Re(count) = (denscalc*D*V(count))/visccalc;
    t(count + 1) = t(count) + h;
    K1Vx = -.5*denscalc*((Vx(count).^2 + Vy(count).^2).^.5)*(Vx(count))*S*Cd;
    K1Vy = -m*g -.5*denscalc*((Vx(count).^2 +
Vy(count).^2).^.5)*(Vy(count))*S*Cd;
    K1X = Vx(count);
    K1Y = Vy(count);
    m = floor((Y(count) + .5*K1Y*h)/2000);
    n = ceil((Y(count) + .5*K1Y*h)/2000);
    k = (Y(count)+ .5*K1Y*h - Alti(m))/(Alti(n)-Alti(m));
    denscalc = Dens(m) + k*(Dens(n)-Dens(m));
    K2Vx = -.5*denscalc*(((Vx(count)+.5*K1Vx*h).^2 +
(Vy(count)+.5*K1Vy*h).^2)^.5)*(Vx(count)+.5*K1Vx*h)*S*Cd;
    K2Vy = -m*g -.5*denscalc*(((Vx(count)+.5*K1Vx*h).^2 +
(Vy(count)+.5*K1Vy*h).^2).^.5)*(Vy(count)+.5*K1Vy*h)*S*Cd;
    K2X = Vx(count) + .5*K1Vx*h;
    K2Y = Vy(count) + .5*K1Vy*h;
    m = floor((Y(count) + .5*K2Y*h)/2000);
    n = ceil((Y(count) + .5*K2Y*h)/2000);
    k = (Y(count)+ .5*K2Y*h - Alti(m))/(Alti(n)-Alti(m));
    denscalc = Dens(m) + k*(Dens(n)-Dens(m));
    K3Vx = -.5*denscalc.*(((Vx(count)+.5*K2Vx*h).^2 +
(Vy(count)+.5*K2Vy*h).^2).^.5).*(Vx(count)+.5*K2Vx*h)*S*Cd;
    K3Vy = -m*g -.5*denscalc.*(((Vx(count)+.5*K2Vx*h).^2 +
(Vy(count)+.5*K2Vy*h).^2).^.5).*(Vy(count)+.5*K2Vy*h)*S*Cd;
    K3X = Vx(count) + .5*K2Vx*h;
    K3Y = Vy(count) + .5*K2Vy*h;
    m = floor((Y(count) + K3Y*h)/2000);
    n = ceil((Y(count) + K3Y*h)/2000);
    k = (Y(count)+ K3Y*h - Alti(m))/(Alti(n)-Alti(m));
    denscalc = Dens(m) + k*(Dens(n)-Dens(m));
    K4Vx = -.5*denscalc.*(((Vx(count)+ K3Vx*h).^2 + (Vy(count)+
K3Vy*h).^2).^.5).*(Vx(count)+ K3Vx*h)*S*Cd;
    K4Vy = -m*g -.5*denscalc.*(((Vx(count)+ K3Vx*h).^2 + (Vy(count)+
K3Vy*h).^2).^.5).*(Vy(count)+ K3Vy*h)*S*Cd;
    K4X = Vx(count) + K3Vx*h;
    K4Y = Vy(count) + K3Vy*h;
    Vx(count + 1) = Vx(count) + h*(K1Vx + 2*K2Vx + 2*K3Vx + K4Vx)/6;
    Vy(count + 1) = Vy(count) + h*(K1Vy + 2*K2Vy + 2*K3Vy + K4Vy)/6;
    V(count + 1) = (Vx(count + 1)^2 + Vy(count + 1)^2)^(0.5);
    X(count + 1) = X(count) + h*(K1X + 2*K2X + 2*K3X + K4X)/6;
    Y(count + 1) = Y(count) + h*(K1Y + 2*K2Y + 2*K3Y + K4Y)/6;
    if Y(count + 1) <= 0
        X(count + 1) = X(count);
        Y(count + 1) = 0;
        Vx(count + 1) = 0;
        Vy(count + 1) = 0;
        V(count + 1) = 0;
    end
end
plot(V,Y)
end
```

WORKS CITED

1.) Carandente, V., R. Savino, M. Iacovazzo, and C. Boffa. "Aerothermal Analysis of a Sample-Return Reentry Capsule." *Fluid Dynamics and Material Processing* 9.4 (2013): 461-84. Web. 20 Sep. 2015.

2.) United States of America. NASA. Marshall Space Flight Center. *An Automated Method to Compute Orbital Re-entry Trajectories with Heating Constraints*. By Curtis Zimmerman, Greg Dukeman, and John Hanson. Huntsville AL: NASA Marshall Space Flight Center, 2003. Web. 20 Sep. 2015.

3.) Adams, John C., Jr. *Atmospheric Re-Entry*. Tech. N.p.: Arnold Engineering Development Center, 2003. Web. 20 Sep. 2015.

4.) Finke, Reinald G. *CALCULATION OF REENTRY-VEHICLE TEMPERATURE HISTORY*. Tech. no. P-2395. Alexandria VA: Institute for Defense Analysis, 1990. Web. 20 Sep. 2015.

5.) Ghislain Tchuen and Yves Burtschell (2011). Physico - Chemical Modelling in Nonequilibrium Hypersonic Flow Around Blunt Bodies, Aeronautics and Astronautics, Prof. Max Mulder (Ed.), ISBN: 978-953-307-473-3,

6.) Yamada, Tetsuya, Yoshifumi Lnatani, Masahisa Honda, and Ken I Ch Hirai. "DEVELOPMENT OF THERMAL PROTECTION SYSTEM OF THE MUSES-C/DASH REENTRY CAPSULE." *Acta Astronautica*51.1-9 (2002): 63-71. Web. 20 Sept. 2015.

7.) Hudson, Troy Lee (2008) *Growth, diffusion, and loss of subsurface ice on Mars: experiments and models.* Dissertation (Ph.D.), California Institute of Technology. Web. 20 Sep. 2015.

8.) Chang, Chau-Lyan, and Balaji S. Venkatachari. *Effect of Counterflow Jet on a Supersonic Reentry Capsule*. Proc. of 42nd AIAA Joint Propulsion Conference and Exhibit, California, Sacramento. Sacramento: AIAA, 2006. Web. 20 Sep. 2015.

9.) Minjie Zhang, Xiang Shuhong, and Tong Jingyu. "FILM COOLING EFFECTIVENESS FOR HYPERSONIC VEHICLES." Proc. of The 22nd International Congress on Sound and Vibration, Italy, Florence. Web. 20 Sep. 2015.

10.) Sandberg, Richard D. *Governing Equations for a New Compressible Navier-Stokes Solver in General Cylindrical Coordinates*. Tech. no. AFM-07/07. Southampton: U of Southampton, 2007. Web. 20 Sep. 2015.

11.) Siva, D., K. Reddy, and Krishnendu Sinha. "Hypersonic Turbulent Flow Simulation of FIRE II Reentry Vehicle Afterbody." *JOURNAL OF SPACECRAFT AND ROCKETS* 46.4 (2009): 745-57. Web. 20 Sep. 2015.

12.) Scott-Pomerantz, Colleen D. *THE K-EPSILON MODEL IN THE THEORY OF TURBULENCE*. Diss. U of Pittsburg, 2004. Pittsburg: U of Pittsburg, 2004. Web. 20 Sep. 2015.

13.) Schneider, Steven P. "Laminar-Turbulent Transition on Reentry Capsules and Planetary Probes." *JOURNAL OF SPACECRAFT AND ROCKETS* 43.6 (2006): 1153-173. Web. 20 Sep. 2015.

14.) Moss, James N., Katie A. Boyles, and Francis A. Greene. "Orion Aerodynamics for Hypersonic Free Molecular to Continuum Conditions." Proc. of 14th AIAA/AHI International Space Planes and Hypersonic Systems and Technologies Conference, Australia, Canberra. N.p., n.d. Web. 20 Sep. 2015.

15.) Balage, Sudantha, Russell Boyce, Neil Mudford, Harshad Ranadive, and Sudhir Gai. "Similarity Laws of Re-Entry Aerodynamics - Analysis of Reverse Flow Shock and Wake Flow Thermal Inversion Phenomena." Proc. of 26th International Symposium on Shock Waves, Germany, Göttingen. Vol. 1. Göttingen: German Aerospace Center, 2007. 689-94. Web. 20 Sep. 2015.